



ISSN 1028-8546

Volume XXV, Number 2

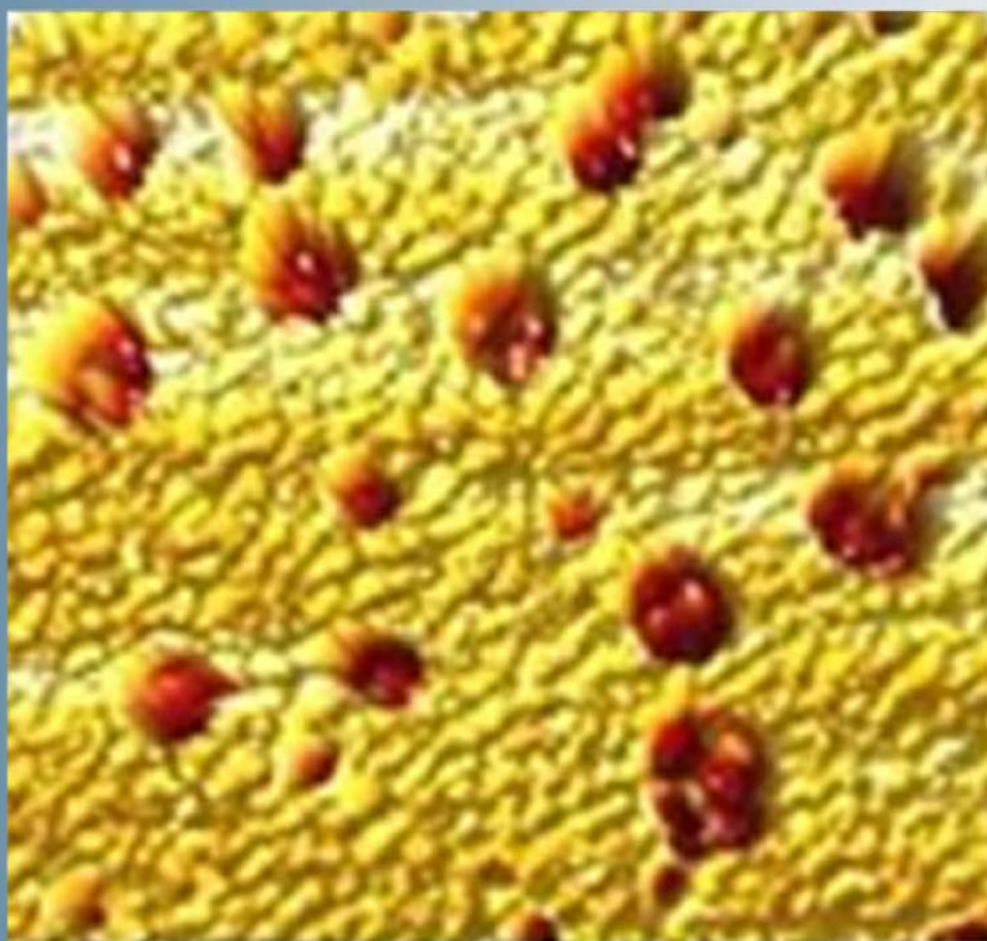
Section: En

July, 2019

Azerbaijan Journal of Physics

Fizika

www.physics.gov.az



G.M. Abdullayev Institute of Physics
Azerbaijan National Academy of Sciences
Department of Physical, Mathematical and Technical Sciences

Published from 1995
Ministry of Press and Information
of Azerbaijan Republic,
Registration number 514, 20.02.1995

ISSN 1028-8546
vol. XXV, Number 02, 2019
Series: En

Azerbaijan Journal of Physics

FIZIKA

*G.M. Abdullayev Institute of Physics
Azerbaijan National Academy of Sciences
Department of Physical, Mathematical and Technical Sciences*

HONORARY EDITORS

Arif PASHAYEV

EDITORS-IN-CHIEF

Nazim MAMEDOV

Chingiz QAJAR

SENIOR EDITOR

Talat MEHDIYEV

INTERNATIONAL REVIEW BOARD

Ivan Scherbakov, Russia
Kerim Allahverdiyev, Azerbaijan
Mehmet Öndr Yetiş, Turkey
Gennadii Jablonskii, Buelorussia
Rafael Imamov, Russia
Vladimir Man'ko, Russia
Eldar Salayev, Azerbaijan
Dieter Hochheimer, USA
Victor L'vov, Israel

Vyacheslav Tuzlukov, South Korea
Majid Ebrahim-Zadeh, Spain
Anatoly Boreysho, Russia
Mikhail Khalin, Russia
Hasan Bidadi, Tebriz, Iran
Natiq Atakishiyev, Mexico
Tayar Djafarov, Azerbaijan
Arif Hashimov, Azerbaijan
Javad Abdinov, Azerbaijan

Bagadur Tagiyev, Azerbaijan
Salima Mehdiyeva, Azerbaijan
Talat Mehdiyev, Azerbaijan
Ayaz Baramov, Azerbaijan
Tofiq Mammadov, Azerbaijan
Shakir Nagiyev, Azerbaijan
Rauf Guseynov, Azerbaijan
Almuk Abbasov, Azerbaijan
Yusif Asadov, Azerbaijan

TECHNICAL EDITORIAL BOARD

Senior secretary Elmira Akhundova, Nazli Guseynova, Sakina Aliyeva, Gulnura Jafarova
Nigar Akhundova, Elshana Aleskerova, Rena Nayimbayeva

PUBLISHING OFFICE

131 H. Javid ave, AZ-1143, Baku
ANAS, G.M. Abdullayev Institute of Physics

Tel.: (99412) 539-51-63, 539-32-23
Fax: (99412) 537-22-92
E-mail: jophphysics@gmail.com
Internet: www.physics.gov.az
<https://jophphysics.wixsite.com/ajpphysics>

Published at "SƏRQ-QƏRB"
17 Ashug Alessger str., Baku
Typographer : Aziz Gulaliyev

Sent for printing on: __.__. 201_
Printing approved on: __.__. 201_
Physical binding: _____
Number of copies: _____ 200
Order: _____

It is authorized for printing:

THE LOW-FREQUENCY DIELECTRIC PROPERTIES OF BENZENE-BROMOBENZENE SYSTEM

S.T. AZIZOV, O.A. ALIYEV, R.G. ABASZADE

G.M. Abdullayev Institute of Physics of Azerbaijan NAS

131, H. Javid ave., Baku, AZ 1143

e – mail: samir_azizov@mail.ru

The complex dielectric constants of benzene-bromobenzene system at frequency 3 MHz in temperature region from 20°C up to 100°C, which overlap the liquid phase, solid phase and phase between lines of liquidus and solidus, are measured by resonance method. The thermodynamic values characterizing the dielectric relaxation process are calculated.

Keywords: dielectric spectroscopy, dielectric constant, dielectric properties of benzene –bromobenzene solutions.

PACS: 61.20. – p; 77.22. – d; 77.22.Gm;

1. INTRODUCTION

The investigation of dielectric properties can significantly add the results of physicochemical analysis that allows us to reveal such peculiarities of molecular thermal motion which can't be revealed with the help of usual technique. Thus, the most total state diagram can be constructed on the base of temperature-concentration dependence of ϵ_0 equilibrium dielectric constant of benzene-bromobenzene system than the diagram by data of thermal analysis [1]. The correctness of this diagram is confirmed by data of nuclear-magnetic resonance (NMR) [2].

2. EXPERIMENTAL PART

The dielectric constants of benzene–bromobenzene system in temperature interval from 20°C up to 100°C at frequency 3 MHz and bromobenzene content in mole fractions 0,086; 0,175; 0,267; 0,361; 0,459 and 0,64 are measured. The dielectric constants ϵ' and absorption indexes ϵ'' on

waves of lengths 4.0 and 2,14 cm at bromobenzene content in mole fractions 0,175; 0,267; 0,361 and 0,64 are also measured in the same temperature interval.

The measurements at frequency 3 MHz are carried out by resonance method. The error of values doesn't exceed 1%. ϵ' and ϵ'' values are measured in micro-wave region by Poly method [3] in liquid phase and by method of short-circuit line [4] at more low temperatures. ϵ' error is 1–2%, ϵ'' is not more 3–5%. All measurements are carried out at continuous cooling with velocity 0,1 deg/min. The physical constants of refined compounds are well agreed with data giving in reference [5].

The temperature dependence curves of equilibrium dielectric constant ϵ_0 for six solutions of benzene-bromobenzene system are shown in fig. 1. The jump changes of ϵ_0 are clearly revealed in all curves. The dependence of temperature on concentration corresponding to these jump changes in limits of test accuracy coincides with state diagram (fig. 2) obtained with the help of thermal analysis [6].

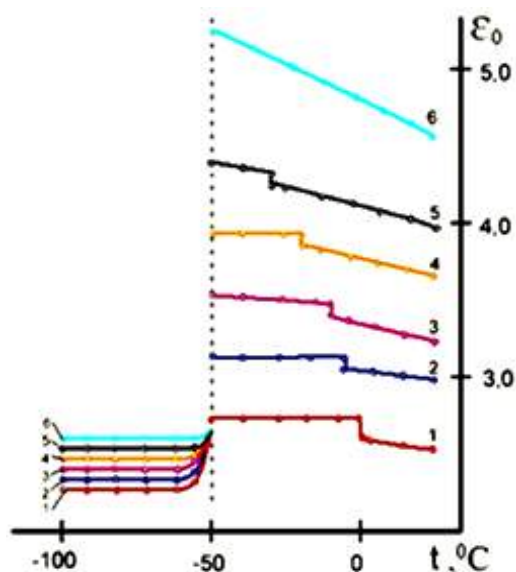


Fig. 1. Temperature dependence of equilibrium dielectric constant ϵ_0 of benzene –bromobenzene solutions at bromobenzene content in mole fractions: 1 – 0,086; 2 – 0,175; 3 – 0,267; 4 – 0,361; 5 – 0,459; 6 – 0,640.

The equilibrium dielectric constant ε_0 increases by jump the value of which increases with the decrease of polar component concentration in points of crystallization beginning. This jump is absent on curve 6 (fig. 1) which corresponds to eutectic concentration. From state diagram it is seen that the jump of equilibrium dielectric constant ε_0 is caused by transition of benzene in solid phase. In this case benzene dielectric constant value is greater than value ε_0 corresponding to liquid phase because of density increase. The benzene crystallization continues with further temperature decrease and composition of liquid phase is added by bromobenzene. The heterogeneities appeared by such way in system bromo-benzene should decrease ε_0 in comparison with values which are expected on the base of data for temperatures higher liquidus line.

The consideration of fig. 1 allows us to emphasize the two temperature region in which molecules of bromo-benzene have definite orientational freedom. In this connection the temperature dependences of dielectric coefficients of investigated solutions on the waves of lengths 4,0 and 2,1 cm are measured, where the main absorption region should be observed [7].

ε' and ε'' values for the solution with content of bromobenzene in molar fractions on the wave of the length 4,0 are shown in fig. 2. From fig. 2 it is seen that the changes in the form of fractures are revealed at the pass through the point of crystallization beginning on the curves. The dispersion below liquidus line significantly shifts to the side of more low frequencies and the small symmetric distribution of relaxation times near the most probable relaxation time τ_0 increasing with temperature decrease.

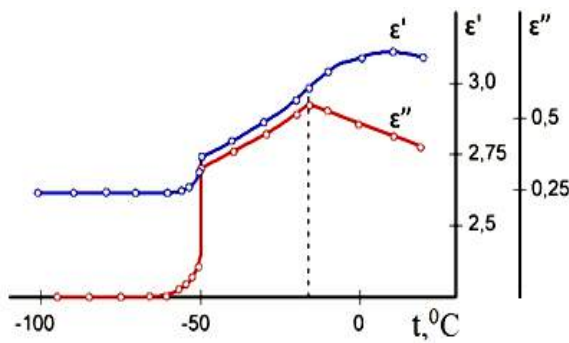


Fig.2. The temperature dependences of dielectric constant ε' and electric absorption index ε'' of benzene - bromobenzene solution in molar fractions 0,267 on the wave length of 4,0 cm.

The frequency dependences in liquidus-solidus interval is found from Cole - Cole equation [8]:

$$\varepsilon^* = \varepsilon' - i\varepsilon'' = \varepsilon_\infty + \frac{\varepsilon_0 - \varepsilon_\infty}{1 + i\omega\tau_0^{1-a}} \quad (1)$$

where ε_∞ is high-frequency dielectric constant, a is parameter of relaxation time distribution, ω is circular

frequency, $i = \sqrt{-1}$.

$a = 0$ higher liquidus line. The times of dielectric relaxation are defined by Cole -Cole graphical method [8].

The activation of dielectric relaxation process can be studied in detail with the help of theory of reaction absolute velocity [9]. In this theory the connection between dielectric relaxation time and activation thermodynamic parameters is established:

$$\tau_0 = \frac{h}{kT} \exp \frac{\Delta F}{RT} = \frac{h}{kT} \exp \frac{\Delta H}{RT} \exp \left(-\frac{\Delta S}{R} \right) \quad (2)$$

where ΔF , ΔH , ΔS are free energy, enthalpy and entropy of activation correspondingly, h is Plank constant, k is Boltzmann constant, R is gas constant, T is absolute temperature.

ΔF value is calculated by the equation:

$$\Delta F = 2,303 RT \lg (2,08 \cdot 10^{10} \tau_0 T) \quad (3)$$

The activation entropy ΔH is found from inclination of $\lg (\tau_0 T)$ dependence on $\frac{1}{T}$ according to equation:

$$\Delta H = 2,303 R \frac{d \lg (\tau_0 T)}{d (1/T)} \quad (4)$$

The activation entropy of ΔS activation is found from the equation:

$$\Delta F = \Delta H - T\Delta S \quad (5)$$

The activation free energy stays the same as in liquid phase because of big growth of ΔH and ΔS .

The observable effects can't be explained by the only one concentration change, i.e. the relaxation times in liquidus-solidus not higher values corresponding electric concentration but they exceed the values for pure bromobenzene (fig. 3). From dielectric measurements it is followed that at temperatures below liquidus line the volume parts taken by liquid phase are characterized by high molecule order the kinetic behavior of which is essentially differ from the one observed in liquid state higher liquidus line.

3. CONCLUSION

The dependence of equilibrium and complex dielectric constants of hypoeutectic solutions of benzene-bromobenzene system on temperature and concentration is studied. The dielectric relaxation times are obtained.

The relaxation of bromobenzene molecules in liquidus - solidus interval where they are in liquid solution is characterized by solid state values.

- [1] *A.F. Skrishevsky*. The structural analysis of liquids and amorphous solids. Moscow: High school, p. 328, 1980.
- [2] *Y.U. Akhadov*. Dielectric properties of binary solutions. Moscow, "Science", p.322, 1977.
- [3] *J.Ph. Poley*. J. Appl. Sci. Res., 4, 337, 1955.
- [4] *Y.U. Akhadov*. Dielectric parameters of pure liquids solutions, Moscow, p. 854, 1999.
- [5] *B. Nickolsky*. "Chemist handbook" in 6 vol., "State Chemistry Publishing", p.6760, 1963.
- [6] *J. Timmermans*. "Constants of binary systems in concentration solute", Phys. Chem. 1, New-York, 1959.
- [7] *S.T. Azizov, O.A. Aliev, R.G. Abbaszade*. International Journal of Latest Research in Science and Technology, vol. 5, issue 4: p.p.58-62, July– August, 2016.
- [8] *K.S. Cole, R.H. Cole*. J. Chem. Phys., 9, 341, 1941.
- [9] *B.Kaussmann, R.Matzky, G.Opel, E.Vogel*. "Second viral coefficient and viscosity coefficient of fluorobenzene vapor and their calculation from lennard-jones-(m-n) equations for the intermolecular potential", Phys. Chem. (Leipzig), vol. 258, p.p.730–742, 1977.

Received: 12.04.2019

ELECTRONIC STRUCTURE OF THE Ge VACANCIES IN GeSe LAYERED SEMICONDUCTOR

Z.A. JAHANGIRLI^{1,2}, B.H. TAGIYEV¹, S.A. NABIYEVA¹

¹*G.M. Abdullayev Institute of Physics of Azerbaijan NAS*

²*Azerbaijan Technical University*

The electronic structure of the cation vacancies in GeSe is evaluated using the self-consistent Green's function method in bases sets of Linear Combinations of Atomic Orbitals (LCAO). The energy states in energy gaps, their origin, orbital content and resonances due to the localized defects are discussed.

Keywords: electronic structure, Green's function method, vacancies, LCAO.

PACS: 71.23.An, 71.55.Ht, 71.15.Ap, 71.15.Dx

Various defects in crystals play an important role in their physical and chemical properties as thermodynamic, electrophysical, optical and kinetic behaviour of semiconductors. At values of temperature and concentration of charge carrier at which many semiconductor devices work, electronic properties of semiconductors especially sensitive to character of various defects and their concentration. The electronic structure of shallow impurities can be described by means of the effective-mass theory [1]. In case of strongly localized defects, the radius of wave function of the defect states appears less or the order of the lattice constant and the effective-mass theory not suitable. Self-consistent Green's function method has been shown [2-5] to be a powerful tool for studying deep-level impurities, electronic structure of point defects and semiconductor surfaces.

In this paper, we have calculated the electronic structure of the ideal Ge(V_{Ge}) vacancies in GeSe using the self-consistent Green's function scattering-theoretical method. Due to the strong anisotropy of the chemical bonds and their physical properties, the GeSe- type A^{IV}B^{VI} crystals have attracted considerable interest [6-11], especially for their potential applications in electronic devices. In the perspectives of fabricating a non-toxic and low-cost photovoltaic system, A^{IV}B^{VI} type crystals has recently received considerable interest as a potential solar cell material. Physical properties of these compounds are suitable for photovoltaic and nanoquantum-well device applications. GeSe layered compounds crystallize in the D_{2h}^{16} space group of orthorhombic symmetry, with eight atoms in the unit cell. In this structure Ge(Se) atom is surrounded by six Se(Ge) atoms, three at a short distance with the interatomic directions almost perpendicular to each other and three at a somewhat larger distance [12].

Let H^0 be the perfect crystal Hamiltonian, U be the defect potential and $H=H^0+U$ is the one-electron Hamiltonian for the perturbed system. The one-particle Green's operator G^0 defined by

$$G^0(E) = \lim_{\varepsilon \rightarrow 0+} (E - H^0 + i\varepsilon)^{-1} \quad (1) \quad \text{where}$$

and the Green's operator G is defined by

$$G(E) = \lim_{\varepsilon \rightarrow 0+} (E - H + i\varepsilon)^{-1} \quad (2)$$

in terms of H are related by Dyson's equation

$$G = G^0 + G^0 U G \quad (3)$$

This equation can be solved formally to obtain

$$G = (I - G^0 U)^{-1} G^0 \quad (4)$$

The eigenvalue of H^0 correspond to the poles in $G^0(E)$, while H has eigenvalue at energies for which H^0 has eigenvalue and at energies where $(I - G^0 U)^{-1}$ has poles in the energy gaps.

From the above equations we obtain,

$$[I - G^0(E) U] \Psi = 0 \quad (5)$$

where Ψ is wave function of the perturbed system. Bound states correspond to the zeros of the determinant

$$D(E) = \text{Det} \| I - G^0 U \| = 0 \quad (6)$$

If Ψ expand in any complete orthonormal set of states φ_a , equation (6) becomes a set of linear algebraic equations

$$\text{Det} [\delta_{\alpha\beta} - (G^0 U)_{\alpha\beta}] = 0 \quad (7)$$

Since a potential U is strongly localized in a nearby of defect, if localized functions to use as a basis set, the order of a determinant of (6) will be determined by the number of nearest-neighbors for which U_{aa} is nonzero.

The change in the density of states within the band continua is given by

$$\Delta N(E) = \frac{1}{\pi} \frac{d\delta(E)}{dE} \quad (8)$$

$$\delta(E) = -\text{arctg} [Im D(E) / Re D(E)]$$

The change in the charge density arising from redistributions in the valence bands is given by the equation

$$\Delta\rho_V = \int_{-\infty}^{E_V} [\rho(E) - \rho^0(E)] dE = \frac{2}{\pi} \text{Im} \int_{-\infty}^{E_V} \{1 - [1 - G^0(E)U]^{-1}\} G^0(E) dE \quad (9)$$

$$\rho^0(E) = -(2/\pi) \text{Im} G^0(E), \quad \rho(E) = -(2/\pi) \text{Im} G(E)$$

where E_V is the top of the valence bands. This equation expresses the change in the charge density $\Delta\rho_V$ through perturbation potential U .

The total change in the charge density is given by the relation

$$\Delta\rho = \Delta\rho_V + \sum_i |\Psi_i\rangle \langle \Psi_i| \quad (10)$$

where Ψ_i are wave functions of the occupied discrete states in the energy gaps.

For self-consistency, the calculation is first done with a trial U . As a trial potential U it is chosen pseudo potential of the vacancy atom equal in magnitude but opposite in sign [13]. The induced change in the charge density is then calculated from equations (10). This charge density is used to obtain a new U in the local-density approximation and calculation is repeated until self-consistency is achieved. The exchange-correlation effects are considered using the Perdew-Zunger scheme [14] as parametrized by Ceperley and Alder. In the charge distribution calculations the irreducible Brillouin zone (BZ) was sampled with 64 k -points using the Monkhorst-Pack [15] scheme. Since neutral defect does not create long-range Coulomb potential, the defect potential is screened completely. As seen from fig. 1, after the self-consistency the defect potential is effectively screened and localized within the space in radius 4.4 a.u., i.e. smaller, than distance up to nearest-neighbors, equal 4.8 a.u.

In order to calculate the Green's function of the ideal crystal, at first we carried out a band structure calculation to determine the energies and Bloch functions by pseudo potential method in plane-wave basis. In our calculations were used non-local ionic pseudopotentials built up in the scheme suggested by Bachelet et al. [13]. Good convergence has been obtained for the band structure calculation with the choice of a kinetic energy cut-off at 16 Rydberg.

In order to represent $G^0(E)$ and U in matrix form, we used a localized basis set consisting of s , p and d functions centered on the central site and the six nearest neighbors. The radial functions were chosen to be Slater orbitals [16]. Radial functions with $\lambda_{Ge}=1.5$, $\lambda_{Se}=1.52$ were used for s functions and with $\lambda_{Ge}=1.8$, $\lambda_{Se}=1.83$ were used for p and d functions. To test convergence the calculations were repeated with additional radial functions, but the results were not essentially changed. We have computed the matrix elements of $G^0(E)$ and U in reciprocal space. For this purpose, we expand the localized orbitals in plane waves. Fourier transform of the Slater orbitals easily derived in an analytical form. Once the expansion coefficients are known, all matrix elements can be calculated in plane-wave representation.

Point group C_{1h} of the cation vacancies consists of: $\{E\}$, identical element; $\{\sigma_v\}$, reflection plane perpendicular to the x axis, passing through vacancy (the axis are chosen as in [17]). Group-theoretical analysis shows that all defect states not degenerate and are either symmetric, or anti-symmetric with respect to the mirror plane.

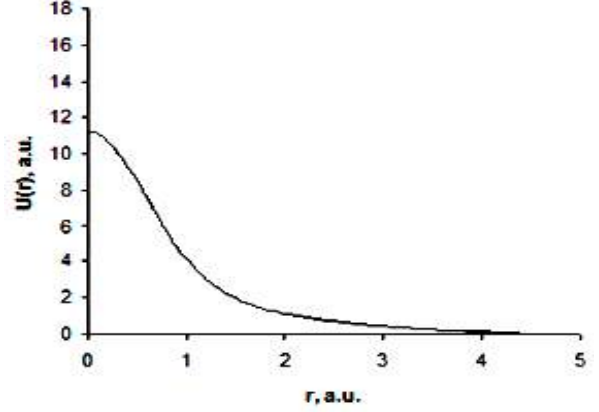


Fig. 1. Screened perturbing potential of V_{Ge} defect.

In fig. 2 we show the calculated charge density of the ideal crystal. The vacancy introduces a repulsive potential corresponding to the removal of an anion or cation potential; as a result states shift to higher energies. The upper valence bands give rise to bound states in the fundamental band gap at $E_V + 0.31$ for V_{Ge} . The lower valence bands about -12 eV give rise to localized state at $E_V + 0.31$ for V_{Ge} . Localized states in the fundamental band gap for both V_{Ge} are empty. Analyzing the character of defect-related wave functions, we find the states in the fundamental band gap to be anti-symmetric while the state at $E_V + 0.31$ is symmetric.

Analysis of the wave functions and charge density associated with the localized states of cation vacancies (fig. 3) reveals that the states in the fundamental gap consist primarily of p -like orbitals centered on the nearest neighbors, whereas the state at about $E_V + 0.31$ consist primarily of s -like orbitals centered on the nearest neighbors and can be characterized as back bonds of the three nearest-neighbour atoms. It is consistent with the fact that the upper valence bands originate mainly from the anion and cation p -states, whereas the lower valence bands originate primarily from anion s -states [7, 17].

The cation vacancy is surrounded by three low-coordinated anion atoms; two in the first layer and one in the second layer. The atomic structure of cation vacancy maintains the C_{1h} symmetry. Wave functions of all deep levels exponentially decay at removal from vacancy. Symmetry and origin of these defect states can be qualitatively explained in terms of LCAO models.

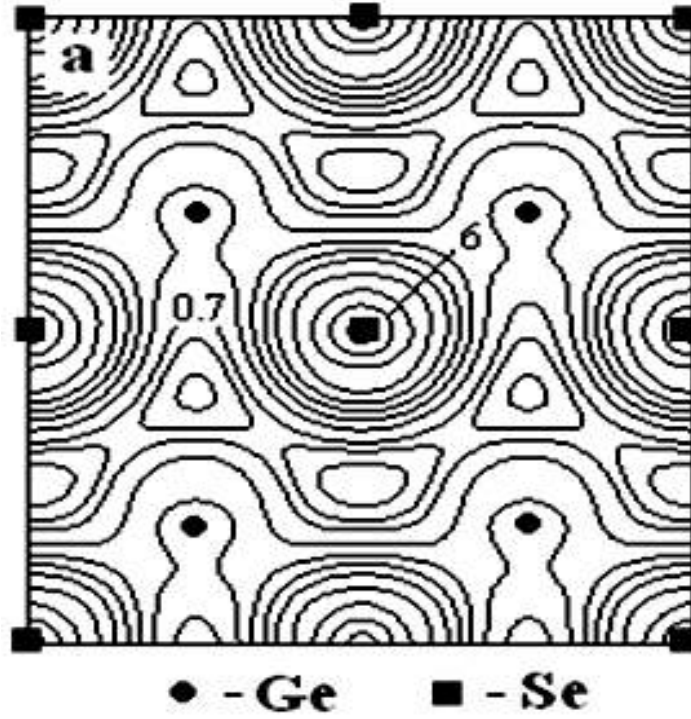


Fig. 2. Charge density in the (010) plane (in electrons per bulk unit cell) for GeSe.

In LCAO models of an ideal crystal [17], using atomic orbitals centered on every atoms it is constructed hybrid orbitals, directed along bonds of the nearest neighbors of the given atom. From this orbitals, then form bonding and anti-bonding orbitals, which give rise to the valence and conduction bands, respectively. For the crystal containing vacancy, the nearest neighbors of vacancy cannot create bonding and anti-bonding orbitals and these orbitals remain "dangling". As a first approximation one would expect that, localized states are linear combinations of these

"dangling hybrids". Actually, our calculations show, that the localized states are primarily a linear combination of these "dangling hybrids".

Except the localized states in the fundamental gap, within the band continua there are defect-induced resonances and anti-resonances. Features at $E_V + 0.31$ eV for V_{Ge} are determined by own nature of defect potential and therefore are resonances. From analyzing the wave functions we find that resonances also consisting mainly of p - states centred at the three neighbours.

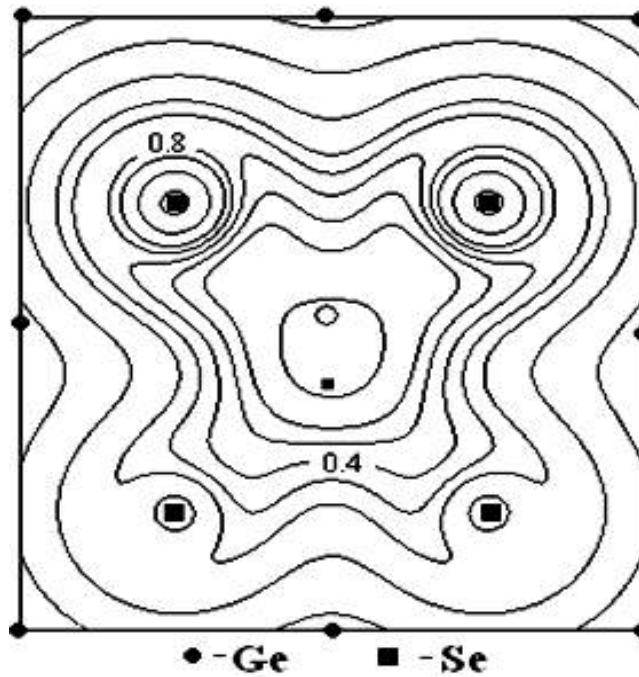


Fig. 3. Charge density in the (010) plane (in electrons per bulk unit cell) associated with the Ge -vacancy.

In accordance with our calculations in [8] it is shown, that presence of cation vacancies in GeSe

cause *p*- type conductivity and formation of impurity states in fundamental band gap.

-
- | | |
|---|--|
| <p>[1] <i>J.M.Luttinger, W.Kohn.</i> Phys. Rev. 97,869, 1955.</p> <p>[2] <i>M.Lannoo, J.Bourgoin.</i> Point defects in Semiconductors, Moscow, Mir, p. 263, 1984.</p> <p>[3] <i>P.Kruger, J.Pollmann.</i> Phys. Rev. B 15, 10578, 1988.</p> <p>[4] <i>J.Bernholc, O.Nunzio, Lipari, S.T.Pantelides</i> Phys. Rev., B 8, 3545, 1980.</p> <p>[5] <i>O.V.Farberovich, A.Yaresko, K.Kikoin, V.Fleurov.</i> Phys. Rev. B 78, 085206, 2008.</p> <p>[6] <i>G.Biswajit, D.Madhumita, B.Pushan, D.Subrata.</i> Semicond. Sci. Technol. 24, 025024, 2009.</p> <p>[7] <i>L.Makinistian, E.A.Albanesi.</i> Phys. Rev. B 74, 045206, 2006.</p> <p>[8] <i>D.I.Bletskan, J.J.Madyar, V.N.Kabaciy,</i> FTP 40, 142, 2006.</p> <p>[9] <i>G.Biswajit, D.Madhumita, B.Pushan, D.Subrata.</i> Semicond. Sci. Technol. 23, 125013, 2008.</p> | <p>[10] <i>S.G.Hickey, C.Waurisch, B.Rellinghaus, A.J.Eychmüller.</i> Am. Chem. Soc. 130, 14978, 2008.</p> <p>[11] <i>Z.A.Jahangirli, M.Z.Zarbaliyev.</i> TJP. 31, 77, 2007.</p> <p>[12] <i>F.M. Gashimzade, V.E. Kharchiev.</i> FTT, 4, 434, 1962.</p> <p>[13] <i>G.Bachelet, D.Hamann.</i> Schluter M. Phys. Rev. B 8, 4199, 1982.</p> <p>[14] <i>J.Perdew, A.Zunger.</i> Phys. Rev. B23, 5048, 1981.</p> <p>[15] <i>H.J. Monkhorst, J.D. Pack.</i> Phys. Rev. B 13, 5188, 1976.</p> <p>[16] <i>D.J. Chadi.</i> Phys. Rev. B 8, 3572, 1977.</p> <p>[17] <i>F.M.Gashimzade,D.G.Guliyev, D.A.Guseinova, V.Y.J.Shteinshrayber.</i> J. Phys.: Condens. Matter, v. 4, p.1081, 1992.</p> |
|---|--|

Received: 17.04.2019

THE STRUCTURAL ANALYSIS AND THERMAL POWER OF $\text{Bi}_2\text{Sr}_2\text{CaCu}_2\text{O}_x$ and $\text{Bi}_2\text{Sr}_2\text{Ca}_{0.6}\text{Zn}_{0.4}\text{Cu}_2\text{O}_x$

S.S. RAGIMOV^{1,2}, G.I. AGAYEVA¹

¹Baku State University, Institute for Physical Problems, Baku, Azerbaijan

²G.M. Abdullayev Institute of Physics of Azerbaijan NAS

131, H. Javid ave., Baku, AZ 1143

e-mail: sadiyar@mail.ru

The temperature dependences of the thermopower of $\text{Bi}_2\text{Sr}_2\text{CaCu}_2\text{O}_x$ and $\text{Bi}_2\text{Sr}_2\text{Ca}_{0.6}\text{Zn}_{0.4}\text{Cu}_2\text{O}_x$ were studied in the temperature range of 77–320 K. It is shown that zinc atoms partially occupy the place of calcium in the CaO planes in the initial matrix. The critical temperature of the transition to the superconducting state for both samples was $T_c=78$ K. The obtained experimental data on the thermopower are analyzed on the basis of a two-band model. It was shown that a partial replacement of the element Ca by zinc leads to a decrease in the width of the forbidden zone. The calculations performed in the framework of the two-band model are in satisfactory agreement with the experiment.

Keywords: superconducting material, thermal power, two-band model

PACS: 74.25.Fy; 74.72.Hs

1. INTRODUCTION

Despite the many studies on HTSC, the nature of superconducting pairing and the mechanisms of scattering of charge carriers in the normal state are still not completely clear. It is also known that the temperature of the superconducting transition T_c in layered HTSCs significantly depends on the degree of doping and reaches its maximum value at the optimum doping value. The introduction of impurities in HTSC leads to a change in the electron system and, as a consequence, to a change in the microscopic parameters of the superconductor.

The study of the thermal power allows us to directly determine the type of conductivity, identify the mechanisms of scattering of charge carriers, determine the degree of their degeneration, calculate such important band parameters as the band gap ε_g , the effective mass of charge carriers m^* [1]. The magnitude and sign of the thermal power in bismuth-based (including yttrium, mercury, and thallium) HTSC cuprates are mainly determined not by the number of CuO_2 planes, but by the carrier concentration in these planes, which can be changed by replacing the basic substance atoms with different elements or by doping with oxygen [2–4].

In this work, we investigated the effects of the zinc element on the thermal power of $\text{Bi}_2\text{Sr}_2\text{CaCu}_2\text{O}_x$ and $\text{Bi}_2\text{Sr}_2\text{Ca}_{0.6}\text{Zn}_{0.4}\text{Cu}_2\text{O}_x$ in the temperature range 77–320 K.

2. EXPERIMENTAL RESULTS AND THEIR DISCUSSION

The studied samples were prepared by the method of solid-phase synthesis, the stoichiometric proportions mixing highly pure powders Bi_2O_3 , CaCO_3 , SrCO_3 , ZnO and CuO . Samples were annealed for 10 hours at 840°C temperature, and then cooled by $1.5^\circ\text{C}/\text{min}$ speed up to room temperature.

X-ray diffraction analysis was performed on Bruker -D8 advance at room temperature with a resolution of $\Delta(2\theta)=0.05^\circ$ in the $5^\circ \leq 2\theta \leq 80^\circ$ interval. The obtained results are shown in fig. 1. As can be seen, additional peaks are observed on the diffractogram with the introduction of the zinc element. Some structural parameters of the studied samples were determined from the data of X-ray structural analysis. The space group of the lattice parameter and the volume of the unit cell of the sample $\text{Bi}_2\text{Sr}_2\text{CaCu}_2\text{O}_x$ are: sp. gr. orthorhombic Pnnn; $a=5,396$, $b=5,395$, $c=30,643$, $V=892.06 \text{ \AA}^3$, respectively.

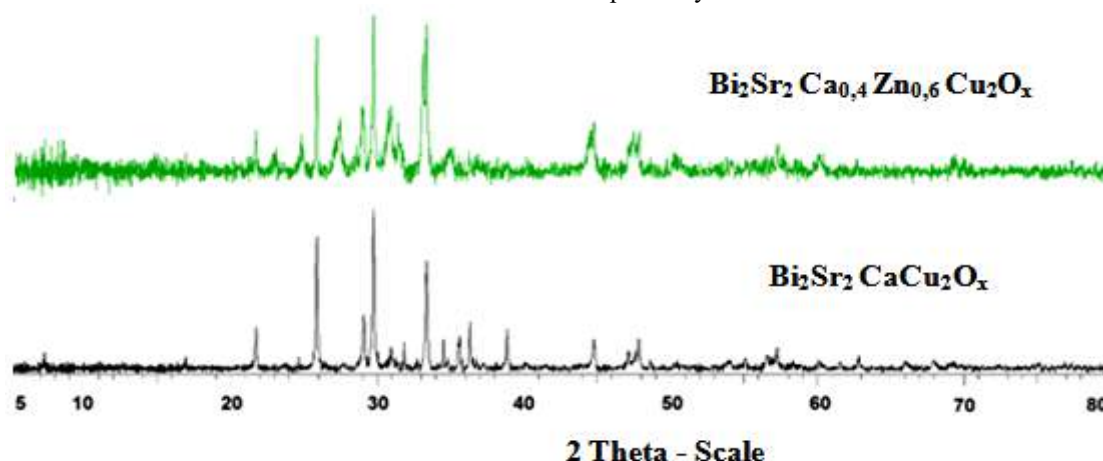


Fig. 1. The X-ray diffractogram of $\text{Bi}_2\text{Sr}_2\text{CaCu}_2\text{O}_x$ and $\text{Bi}_2\text{Sr}_2\text{Ca}_{0.6}\text{Zn}_{0.4}\text{Cu}_2\text{O}_x$

The $\text{Bi}_2\text{Sr}_2\text{Ca}_{0.6}\text{Zn}_{0.4}\text{Cu}_2\text{O}_x$ sample consists of two phases: orthorhombic Pnnn with lattice parameters $a=5,429$, $b=5,431$, $c=30,840$, $V=909.31 \text{ \AA}^3$, and tetragonal I4/ mmm with lattice parameters, $a = 3.8097$, $c = 24.607$, $V = 357.14 \text{ \AA}^3$. According to the intensities of the diffraction peaks, the tetragonal phase prevails.

If we take into account the data of the lattice parameters $\text{Bi}_2\text{Sr}_2\text{ZnCu}_2\text{O}_x$ equal to I4 $a = 3.797 \text{ \AA}$; $b = 24.577 \text{ \AA}$; $V = 354.42 \text{ \AA}^3$ it can be seen that the lattice parameters decrease when the calcium element is replaced with zinc. This is due to the fact that zinc atoms do not fully occupy the corresponding places of the calcium element. Therefore, in the studied compositions, additional diffraction peaks are observed that do not correspond to the initial composition of $\text{Bi}_2\text{Sr}_2\text{CaCu}_2\text{O}_x$. On the other hand, zinc has a smaller ionic radius than calcium (1.04 \AA and 0.83 \AA , respectively). When Ca is replaced by Zn, the crystal structure deforms, similar to that arising under external pressure, as a result of which the lattice parameter decreases [5].

The thermal power was measured by the standard four-contact method in a zero magnetic field. Electrical contacts were applied with indium. The fig. 2 shows the results of the temperature dependences of the thermal power of the studied samples. As can be seen, the temperature dependences of the thermal power pass through a maximum before the phase transition. In both cases, the thermal power value decreases with increasing temperature. The character of the $S(T)$ curves for both studied samples is the same and indicates the hole type of conductivity in the studied temperature interval. However, there is a clear tendency to change the sign of conductivity with increasing temperature. This indicates that two types of charge carriers are involved in conduction; both holes and electrons. To explain the temperature dependence, we used the Xin model [6].

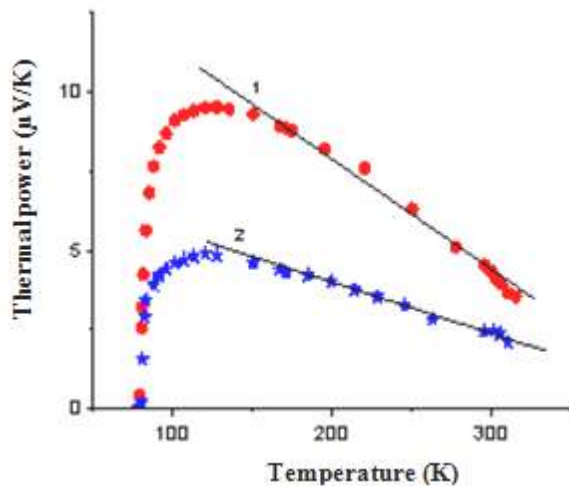


Fig. 2. The temperature dependences of thermal power of $\text{Bi}_2\text{Sr}_2\text{CaCu}_2\text{O}_x$ (1) and $\text{Bi}_2\text{Sr}_2\text{Ca}_{0.6}\text{Zn}_{0.4}\text{Cu}_2\text{O}_x$ (2)

The two-band model of Xin is based on structural-zone calculations, which suggest that the metallic conductivity is due to Cu -O planes, and the

Bi -O zone ($\text{Bi}_{6p}-\text{O}_{2p}$) affects the Fermi energy E_f and the Fermi surface of the HTS material. In the Bi-O planes, electron conductivity takes place, while hole conductivity dominates in the Cu-O plane. A decrease in the valence state of Bi^{3+} to $\text{Bi}^{3-\delta}$ leads to an increase in the electron conductivity in the Bi-O plane, while the oxidation of Cu^{2+} to $\text{Cu}^{2+\delta}$ increases the hole conductivity of the Cu -O planes.

As is known, in the case of two types of charge carriers, S can be represented as:

$$S = \frac{\sigma_p}{\sigma_n + \sigma_p} S_p + \frac{\sigma_n}{\sigma_n + \sigma_p} S_n \quad (1)$$

where S_p and S_n are thermal power due to holes and electrons; $\sigma_p = e p \mu_p$, $\sigma_n = e n \mu_n$, μ_p , μ_n , p , n – are the conductivity, mobility, and concentration of holes and electrons, respectively. This formula is fairly general and independent of the specifics of the mechanism for the appearance of the thermal power [1].

If we assume that the metallic conductivity of the valence band is inversely proportional to temperature, i.e. $\sigma \sim 1/T$, and the conductivity of electrons in the conduction band is a classical semiconductor type

$$\sigma \sim \exp(-E_c/kT) \quad (2)$$

Then the thermal power in some approximation can be expressed as

$$S = AT + (B\lambda + CT) \exp(-\lambda/T) \quad (3)$$

where the parameter A depends on the contribution of mobile holes from the Cu-O planes, B and C are constant. Note that the increase in the value of the parameter A is due to a decrease in the hole concentration, which in turn depends on the oxygen content in these samples. Regarding the parameter λ , we can say that it depends on the energy gap between the Bi-O and the conduction band.

Calculations of thermal power were carried out on the basis of relation (3). The obtained data are presented in the fig. 2 by solid lines in comparison with the experimental curves $S(T)$. The parameters used in the calculations for these studied samples were respectively equal: for $\text{Bi}_2\text{Sr}_2\text{CaCu}_2\text{O}_x$ ($A=0,3 \text{ mkV/K}^2$, $B= -0,5 \text{ mkV/K}^2$, $C=0,2$ and $\lambda=545$), and for $\text{Bi}_2\text{Sr}_2\text{Ca}_{0.6}\text{Zn}_{0.4}\text{Cu}_2\text{O}_x$ ($A = 0,36 \text{ mkV/K}^2$, $B= -0,45 \text{ mkV/K}^2$, $C = 0,2$ and $\lambda=520$). As can be seen, the value of the parameter A increases in the case of substitution by the element Zn. Note that the parameter A is associated with the contribution of mobile holes in the Cu -O planes. Thus, in this case, an increase in the value of the parameter A in $\text{Bi}_2\text{Sr}_2\text{Ca}_{0.6}\text{Zn}_{0.4}\text{Cu}_2\text{O}_x$ indicates a decrease in the hole concentration. As can be seen from the fig. 2, the calculations performed are in satisfactory agreement with the experiment.

The calculated values of the coefficient λ for the studied samples also differ. Since λ depends on the energy gap, its decrease is due to a decrease in the width of the forbidden band. We believe that this may be due to the presence of $\text{Bi}_2\text{Sr}_2\text{Ca}_{0.6}\text{Zn}_{0.4}\text{Cu}_2\text{O}_x$ in the

sample compared with $\text{Bi}_2\text{Sr}_2\text{CaCu}_2\text{O}_x$ slightly greater number of defects, which leads to a decrease in the width of the forbidden zone. Note that the critical temperature of the transition to the superconducting state according to the resistivity data for both samples was $T_c = 78.2$ K. This is due to the fact that Zn atoms partially occupy the place of calcium in the CaO planes in the original matrix.

On the other hand, a change in the lattice parameters leads to a significant change in the SC parameters due to a change in the distances between the superconducting planes and dielectric blocks, as well as due to the redistribution of the charge between them. As can be seen from fig. 2, with inclusion element Zn, the value of thermal power decreases. Note that the resistance of the samples may increase

either by increasing the number of defects or by decreasing the density of charge carriers. It is possible that in this case both mechanisms take place. The replacement of Ca by Zn leads to the formation of defects in the crystal structure of the sample.

3. CONCLUSION

The replacement of Ca with Zn leads to the formation of defects in the crystal structure of the superconducting $\text{Bi}_2\text{Sr}_2\text{Ca}_{0.6}\text{Zn}_{0.4}\text{Cu}_2\text{O}_x$. The experimental data on the thermal power are analyzed on the basis of a two-band model and was shown that a partial replacement of the element Ca by Zn leads to a decrease in the width of the forbidden zone.

-
- [1] *L.S. Stilbans.* Semiconductors Physics, M., Soviet radio, p. 452, 1967 (in Russian).
- [2] *M. Pekala, K. Kitazawa, A. Polaczek et al.* Anisotropy thermoelectric power and thermal conductivity in superconducting single crystals Bi-Ca-Cu-O. Solid State Communations, v. 76, № 3, p. 419 -421, 1990.
- [3] *S.S. Ragimov, A.A. Saddinova, V.M. Aliev, R.I. Selim-zade.* The influence of fluctuations on the superconducting properties of $\text{Bi}_2\text{Sr}_2\text{Ca}_{0.6}\text{Zn}_{0.4}\text{Cu}_2\text{O}_x$ and $\text{Bi}_2\text{Sr}_2\text{Ca}_1\text{Cu}_2\text{O}_x$, Materials Science Forum, v. 845, p. 17-20, 2016.
- [4] *E.S. Itskevich, V.F. Kraidenov, I.G. Kuzemskaya* JETG, vol. 118, №3 (9), p.p. 647-653, 2000.
- [5] *S.S. Ragimov, I.N. Askerzade, G.I. Agayeva.* Journal of Superconductivity and Novel Magnetism, N1, doi.org/10.1007/s10948-019-5010-y., 2019.
- [6] *Y. Xin, K. Wong, C. Fan et al.* Thermoelectric power of the thallium-based superconductor $\text{Tl}_2\text{Ba}_2\text{Ca}_2\text{Cu}_3\text{O}_{10-x}$, J. Phys. Rev. B, v.48, №1, p. 557-560, 1993-I.

Received: 22.04.2019

THE SEMICONDUCTORS WITH DEEP TRAPS IN STRONG ELECTRIC AND MAGNETIC FIELDS

E.R. GASANOV, Sh.G. KHALILOVA

G.M. Abdullayev Institute of Physics of Azerbaijan NAS

131, H. Javid ave., Baku, Azerbaijan, AZ 1143

The energy radiation with different values of radiation frequencies takes place in the semiconductors with definite deep traps and both signs of charge carriers in electric and magnetic fields. The values of electric field strength at magnetic one $\mu_{\pm}H \gg C$ are defined for each case. The sign of the scattering constant of charge carrier is defined. The analytical expressions for the parameters of recombination and generation of charge carriers β_{\pm}^{γ} are found. The current oscillation theory is constructed in linear approximation. The values of $(\omega_1, \omega_2, \omega_3)$ frequency and (E_1, E_2, E_3) strength of the electric field are well agree with existing experimental data. The given semiconductors can be used at the preparation of generators and amplifiers.

Keywords: semiconductors, impedance, ohmic resistance, frequency, Coulomb barrier.

PACS: 72.70.m, 72.70.+m, 73.40.Gk, 73.40.Jn, 73.40.Mr, 73.43.Jn.

1. INTRODUCTION

The current oscillation theory in semiconductors with deep traps and two types of charge carriers is described in works [1-5]. The following constants $\beta_{\pm}^{\gamma} = 2 \frac{d\ln\gamma_{\pm}U}{d\ln(E_0^2)}$, $\beta_{\pm}^{\mu} = 2 \frac{d\ln\gamma_{\pm}\mu_{\pm}}{d\ln(E_0^2)}$ are taken as the positive ones in the given works.

However, below we will show that β_{\pm}^{μ} can be negative values in the dependence on scattering character of charge carriers and β_{\pm}^{γ} constants stay positive ones.

In this theoretic work we will construct the oscillation current theory in the semiconductors with concrete deep traps and two types of charge carriers in strong electric $v_d > S$ and magnetic $\mu_{\pm}H_0 \gg C$ fields at $\beta_{\pm}^{\mu} < 0$.

The drift velocity of charge carriers v_d is defined by formula $v_d = \mu_{\pm}E_0$ where μ_{\pm} are mobilities of holes and electrons, E_0 is strength of constant electric field, H_0 is strength of external magnetic field, S is velocity of sound in the crystal.

For β_{\pm}^{γ} constants we obtain the analytical expressions as the functions of electric fields, magnetic fields, oscillation current frequencies.

2. SEMICONDUCTOR MODEL AND TASK MAIN EQUATIONS

The electrons (and also holes) at the existence of

electric field receive the energy of eE_0l order (e is positive elementary charge; l is length of electron free path).

That's at existence of electric field the electrons can overcome Coulomb barrier of singly charged center and recombine with this center.

Besides, as a result of heat transfer process, the electrons can regenerate from impurity centers (from deep traps) to the conduction band. The capture process decreases the electron number and transfer process increases it in conduction band.

The number of holes increases because of electron capture by deep traps from valence band and decreases because of the electron capture by the holes from deep traps. The different probabilities of generation and recombination lead to carrier concentration change in the crystal. We will mind that the semiconductor with carriers of both signs, i.e. electrons and holes with concentrations n_- and n_+ correspondingly. Besides, the negatively charged deep traps with N_0 concentration from which N is concentration of singly negatively charged traps and N_- is concentration of double negatively charged traps

$$N_0 = N_+N_- \quad (1)$$

The continuity equation for the electrons in the semiconductors with above mentioned types of the traps has the form:

$$\frac{\partial n_0}{\partial t} + \text{div}j_- = \gamma_-(0)n_{1-}N_- - \gamma_-(E)n_-N = \left(\frac{\partial n_-}{\partial t}\right)_{\text{rec}} \quad (2)$$

Here and further j_{\pm} are flux densities of electrons and holes, $j_{-(0)}$ is radiation value of electrons by double negatively charged traps in the absence of electric field. It can be called the coefficient of thermal generation coefficient. $\gamma_-(E)$ is coefficient of electron capture by singly negatively

charged traps at the presence of electric field. $\gamma_-(E) = \gamma_-(0)$ at $E=0$.

In (2) the unknown constant n_{1-} having the concentration dimension, is defined by the following method. At the absence of electric field and under stationary and equilibrium conditions,

i.e. $(\frac{\partial n_-}{\partial t})_{rec} = 0$ and $\gamma_-(E) = \gamma_-(0)$ we obtain from (2):

$$n_{1-} = \frac{n_-^0 N_0}{N_-^0}$$

The electron flux density at the presence of electric and magnetic fields is determined by the expression:

$$\vec{j}_- = -n\mu(E, H)\vec{E} + n\mu_{1-}(E, H)[\vec{E}\vec{h}] - n\mu_2(E, H)\vec{h}(\vec{E}\vec{h}) - D_- \vec{\nabla} n + D_{1-}[\vec{\nabla} n \vec{h}] - D_2 \vec{h}(\vec{\nabla} n \vec{h}) \quad (3)$$

Here \vec{h} is unit vector along magnetic field, $\mu(E, H)$ is ohmic electron mobility, $\mu_{1-}(E, H)$ is Hall electron mobility, $\mu_2(E, H)$ is focused electron mobility, D_-, D_{1-}, D_{2-} are ohmic, Hall, focused electron diffusion coefficients correspondingly. For the simplifying of big calculations we consider the case when the carriers have the effective temperature. Then diffusion coefficient is:

$$D_{\pm} = \frac{T_{ef}}{e} \mu_{\pm}, \quad T_{ef} = \frac{T}{3} \left(\frac{CE_0}{SH_0} \right)^2 \quad [6]$$

C is speed of light in the crystal, T is temperature in energy units. Besides, we will consider the crystals the sizes of which satisfy to following relations:

$$L_y \ll L_x, \quad L_z \ll L_x$$

The continuation equation for the holes has the form:

$$\frac{\partial n_+}{\partial t} + \text{div} j_+ = \gamma_+(E)n_{1+}N_+ - \gamma_+(0)n_+N_- = \left(\frac{\partial n_-}{\partial t} \right)_{rek} \quad (4)$$

$$\vec{j}_+ = n_+\mu_+(E, H)\vec{E} + n_+\mu_{1+}(E, H)[\vec{E}\vec{h}] - n_+\mu_2(E, H)\vec{h}(\vec{E}\vec{h}) - D_+ \vec{\nabla} n_+ + D_{1+}[\vec{\nabla} n_+ \vec{h}] - D_{2+} \vec{h}(\vec{\nabla} n_+ \vec{h})$$

At $E = 0$, $\gamma_+ = \gamma_+(0)$, $n_{1+} = \frac{n_+^0}{N_0}$

As a result of recombination and generation in non-stationary conditions the number of single and double negatively charged traps changes (the general concentration of traps stay constant). The change of the number of double negatively charged traps by the time defines the change of the number single negatively charged traps by the time has the form:

$$\frac{\partial N_-}{\partial t} = \left(\frac{\partial n_+}{\partial t} \right)_{rec} - \left(\frac{\partial n_-}{\partial t} \right)_{rec} \quad (5)$$

The external electric field is directed along X axis and magnetic field is directed along Z axis. Suppose that:

$$n_{\pm}(\vec{r}_1 t) = n_{\pm}^0 + \Delta n_{\pm}(\vec{r}_1 t), \quad N_{\pm}(\vec{r}_1 t) = N_{\pm}^0 + \Delta N_{\pm}(\vec{r}_1 t), \quad \vec{E}(\vec{r}, t) = \vec{E}_0 + \Delta \vec{E}(\vec{r}, t) \quad (6)$$

The inclination of magnetic field from equilibrium value is equal to 0 as we consider the longitudinal oscillations. (0) sign meaning the equilibrium value of corresponding values we will not write.

Let's linearize the equations (2) and (4) taking into consideration (6) and introduce the following character frequencies:

$$v_- = \gamma_-(E_0)N_0, \quad v_+ = \gamma_+(0)N_-^0, \quad v_+^E = \gamma_+(E_0)N_0, \quad v_- = \gamma_-(E_0)n + \gamma_-(v)n_{1-}, \\ v_+ = \gamma_+(0)n_+ + \gamma_+(E_0)n_{1+}$$

and designate the numerical constants defining the dependences on electric field $\gamma_{\pm}(E_0)$ and $\mu_{\pm}(E_0)$

$$\beta_{\pm}^{\gamma} = 2 \frac{d \ln \gamma_{\pm}(E_0)}{d \ln(E_0^2)}; \quad \beta_{\pm}^{\mu} = 2 \frac{d \ln \mu_{\pm}(E_0)}{d \ln(E_0^2)} \quad (7)$$

β_{\pm}^{γ} is dimensionless parameter, β_{\pm}^{γ} can have the negative sign, i.e. $\beta_{\pm}^{\gamma} < 0$ in the dependence on charge carrier scattering. In [7] it is shown that $\beta_{\pm}^{\gamma} = -0,8$ at scattering on optical and acoustic (mixed

scattering) photons $\beta_{\pm}^{\gamma} = -0,8$. We will consider that $\beta_{\pm}^{\gamma} < 0$ in following theoretical calculations.

At absence of recombination and generation of carriers the condition of quazi -neutrality means that the number of electron changes is equal to the number of hole change, i.e. $\Delta n_- = \Delta n_+$. At presence of recombination and generation of charge carriers the condition of quazi-neutrality means that total current doesn't depend on coordinates but depends on time.

$$\text{div} \vec{j} = e \text{div} \left(\vec{j}_+ - \vec{j}_- \right) = 0 \quad (8)$$

After linearization of equations (2), (4), (8) we will obtain the equation for electric field of the following type:

$$\overrightarrow{\Delta E} = a_1 \overrightarrow{\Delta J} + \overrightarrow{a_2} \Delta n_- + \overrightarrow{a_3} \Delta n_+ \quad (9)$$

where a_1, a_2, a_3 are constant values depending on oscillation frequency, character frequencies, equilibrium values of charge carrier concentration, electric and magnetic fields and numerical multipliers $\beta_{\pm}^{\gamma}, \beta_{\pm}^{\mu}$. Because of big coefficients $a_1, \vec{a}_2, \vec{a}_3$ we write only the solution scheme.

Let's divide the functionals $\Delta n_{\pm}(\vec{r}, t)$, $\Delta N_{\pm}(\vec{r}, t)$, $\Delta E(\vec{r}, t)$ to parts proportional to oscillation current ΔJ in external circuit:

$$\Delta n_{\pm}(\vec{r}, t) = \Delta n'_{\pm} e^{i(\vec{k}\vec{r} - \omega t)} + \Delta n''_{\pm} e^{-i\omega t} \quad (10)$$

The analogous divisions we make for ΔN_{\pm} , ΔE . After simple algebraic calculations from (2, 4, 8, 9) taking into consideration (10), we will obtain two equation systems:

$$\begin{cases} d''_- \Delta n''_- + d''_+ \Delta n''_+ = d \Delta J \\ b''_- \Delta n''_- + b''_+ \Delta n''_+ = b \Delta J \end{cases} \quad (11)$$

$$\begin{cases} d'_- \Delta n'_- + d'_+ \Delta n'_+ = 0 \\ b'_- \Delta n'_- + b'_+ \Delta n'_+ = 0 \end{cases} \quad (12)$$

From solution (11) we obtain $\Delta n''_-$ and $\Delta n''_+$. The wave vectors we find from dispersion equation:

$$d'_- b'_+ + b'_- d'_+ = 0 \quad (13)$$

We write (10) in the following form:

$$\Delta n_{\pm}(\vec{r}, t) = \sum_{j=1}^4 \lambda_{\pm}^j e^{i(k_j - r_i)} + \Delta n''_{\pm} e^{-i\omega t} \quad (14)$$

where k_j is dispersion equation root (13).

λ_{\pm}^j are constants are defined from following boundary conditions:

$$\Delta n_{\pm}(0) = \delta_{\pm}^0 \Delta J, \quad \Delta n_{\pm}(L_x) = \delta_{\pm}^{L_x} \Delta J \quad (15)$$

After it we calculate the impedance Z :

$$Z = \frac{\Delta V}{\Delta J} = \frac{1}{\Delta J} \int_0^{L_x} E(x, t) dx = ReZ + ImZ \quad (16)$$

$$\begin{aligned} \frac{ReZ}{Z_0} = & x_+^2 \left\{ 1 + \varphi \left[(\cos \alpha - 1) + \frac{v_-}{\omega \beta_+^{\mu}} \sin \alpha \right] + \varphi_+ (\cos \alpha) - \right. \\ & \left. - \frac{ev\delta x}{\theta} \beta_+^{\mu} \left(\frac{\mu_+}{\mu_-} \right) \sin \alpha - \left(1 + \frac{v_-^2}{\omega^2} \right) \left[\frac{\mu_+}{\beta_+^{\mu} \beta_-^{\mu} \mu_-} + \frac{v_+}{\beta_+^{\mu} \omega \mu} \sin \alpha \right] \varphi_+ \right\} \end{aligned} \quad (17)$$

$$\frac{ImZ}{Z_0} = \frac{x_+}{\theta} \left[B n_+ v_+^E \mu_+ \beta_+^{\gamma} \left(1 + \frac{v_-^2}{\omega^2} \right) - B n_- v_- \mu_- \beta_-^{\gamma} \left(1 + \frac{v_+^2}{\omega^2} \right) + \frac{ev\delta x_+}{2} \left(\frac{\mu_+}{\mu_-} \right)^2 \cos \alpha \right] \quad (18)$$

Here $\delta = \delta_+^0 + \delta_-^0 + \delta_+^{L_x} + \delta_-^{L_x}$, $v = (\mu_- + \mu_+) E_0$, $Z_0 = \frac{L_x}{\sigma_0 S}$, $\sigma_0 = e(n_- \mu_- + n_+ \mu_+)$, S is sample cross-section.

$$\begin{aligned} \theta = & \frac{2L_x v_-}{n_0 k_y v^2 \left(1 + \frac{\beta_+^{\mu}}{\mu_+^{\mu}} \right)} \left(n_+ v_+^E \beta_+^{\gamma} + n_- v_- \frac{\beta_+^{\mu}}{\beta_-^{\mu}} \beta_-^{\gamma} \right); n_0 = n_+ + n_- , \varphi_- = \frac{2n_- v_- \omega^3}{n_0 \omega_1^4 x_+ \theta} \beta_-^{\gamma} , \\ \varphi_+ = & \frac{2n_+ v_+ \omega^3}{n_0 \omega_1^4 x_+ \theta} \beta_+^{\gamma} , \omega_1^4 = \omega^2 (v_-^2 + v_+^2) + \omega^4 + v_-^2 v_+^2 , x_+ = \frac{\mu_+ H}{c} \gg 1 , k_y = \frac{2\pi}{L_y} \end{aligned}$$

We use the following known expressions of mobilities in strong magnetic field:

$$\begin{aligned} \mu_{\pm}(H) = & \left(\frac{c}{H} \right)^2 \cdot \frac{1}{\mu_{\pm}^0} ; \mu_{1\pm} \approx \sqrt{2} \frac{c}{H} ; \\ \mu_{2\pm} \approx & \mu_{\pm}^0 \end{aligned} \quad [9]$$

When the current oscillations in external chain begin so the sample Volt-ampere characteristics becomes linear one. The real part of impedance ReZ has the

negative sign. The impedance imaginary part ImZ can have any sign. Adding to R ohmic resistance from equation solution:

$$-\frac{ReZ}{Z_0} + R = 0 \quad (19)$$

$$\frac{ImZ}{Z_0} + \frac{R_1}{Z_0} = 0 \quad (20)$$

we will find the electric field at which the current oscillations in circuit takes place.

From (18) let's express β_+^Y through β_-^Y .

$$\beta_+^Y = \frac{n_- v_- \mu_-}{n_+ v_+^E \mu_+} \cdot \frac{\omega^2 + v_+^2}{\omega^2 + v_-^2} \beta_-^Y \quad (21)$$

$$\text{then } \frac{ImZ}{Z_0} = \frac{ev\delta\beta_-^\mu}{2} \left(\frac{\mu_+ x_+}{\mu}\right)^2 \cos\alpha \quad (22)$$

Rewrite (17) in the following form:

$$\beta_+^Y = \frac{X_+^2}{A_+ \left[1 + \frac{v_+}{\omega} \left(\frac{\omega + v_-}{v_- + \omega}\right)\right]}, \quad \beta_-^Y = \frac{X_+^2 \left(1 + \frac{v_-^2}{\omega^2}\right)}{A_- \left(\frac{v_- v_+}{\omega^2} + \frac{v_-^2}{\omega^2} + 1\right)} \quad (24)$$

$$A_+ = \frac{2n_0 v_+^E a x_+ \mu_+}{n_0 \omega \theta \beta_+ \mu_-}; \quad A_- = \frac{2n v_- a x_+}{n_0 \omega \theta \beta_+ \mu_-}; \quad a = \frac{\omega^4}{\omega^4}$$

$$\omega_1^4 = \omega^4 + \omega^2(v_-^2 + v_+^2) + v_-^2 v_+^2$$

Equating the ratios $\frac{\beta_+^Y}{\beta_-^Y}$ from (21) and (24) we obtain the following equations for the definition of current oscillation frequency in circuit.

$$y^3 + \frac{v_-}{v_+} y^2 - \frac{v_-^2}{v_+^2} y + \frac{\mu_-}{\mu_+} = 0, \quad y = \frac{\omega}{(v_- v_+)^{1/2}} \quad (25)$$

The analysis of solution of equation shows that the roots of equation (25) have the following form at $v_- > v_+$:

$$Y_3 = -\frac{v_-}{2v_+}(\sqrt{5} + 1), \quad Y_2 = \frac{v_-}{2v_+}(\sqrt{5} - 1), \quad Y_1 = 1 \quad (26)$$

From equation $\frac{ImZ}{Z_0} + \frac{R_1}{Z_0} = 0$ we obtain:
 R_1 is resistance of capacity or inductive character

$$\cos\alpha = -\frac{R_1}{Z_0} \frac{2}{ev\delta} \left(\frac{\mu}{\mu_x X_+}\right)^2 \quad (27)$$

Substituting $\cos\alpha$ from (27) into equation $\frac{ReZ}{Z_0} + \frac{R}{Z_0} = 0$ we obtain the expressions for electric field at the presence of current oscillation in circuit.

$$E_0(\omega_1) = E_1 = \frac{|R_1| \mu}{R |\beta_-^\mu| \mu_+} \cdot \frac{1}{ev\delta}$$

$$E_2 = \frac{4|R_1|}{R |\beta_-^\mu| \mu_-} \cdot \frac{1}{ev\delta} \frac{v_-}{v_+} = E_2$$

3. CONCLUSION

In above mentioned semiconductors the waves with frequencies $\omega_1 < \omega_2 < \omega_3$ at electric fields $E_1 < E_2 < E_3$ are excited (fig.1).

$$\frac{ReZ}{Z_0} = \Phi_0 + \Phi_1 \sin\alpha + \Phi_2 \cos\alpha \quad (23)$$

Using (23) we obtain β_+^Y and β_-^Y by the following way:

$\Phi_0 = 0, \Phi_1 = 0$, then we easily obtain:

Analytical expressions for current oscillation frequencies and for electric field show that constants of charge carrier scattering constants β_\pm^μ have the negative sign.

At current oscillations the resistance of negative character appears in the chain if $R = |R_1|$, $\frac{\mu}{\mu_+} \approx 10$, $\frac{v_-}{v_+} \sim 10$, $ev\delta \sim 10^{-1}$. Then we have:

$$E_1 \sim 10^3 \text{ V/cm}, \quad E_2 \sim 4 \cdot 10^3 \text{ V/cm};$$

$$E_3 \sim 6 \cdot 10^3 \text{ V/cm}.$$

These values are well agree with existing experiments. The corresponding current oscillation frequencies have the following values:

$$\omega_1 \sim 3 \cdot 10^7, \quad \omega_2 \sim \frac{\sqrt{5}-1}{2} \cdot 10^9 \frac{1}{\text{cek}},$$

$$\omega_3 \sim \frac{\sqrt{5}+1}{2} \cdot 10^9 \frac{1}{\text{cek}}$$

It means that the high-frequency current oscillations, i.e. high-frequency radiation of energy from above mentioned semiconductor takes place. The magnetic field is defined from inequality $\mu_\pm H \gg C$. For the definition of region of electric field change and current oscillation frequency at further increase of electric field one can construct the nonlinear theory.

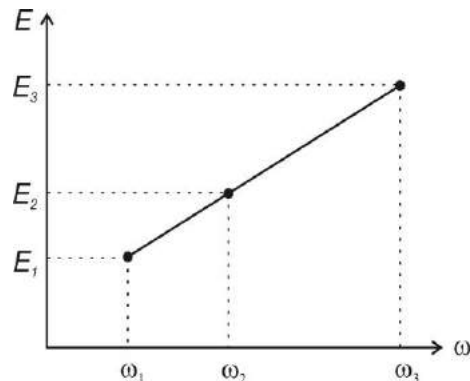


Fig.1. The dependence of electric field on current oscillation frequency.

1. *E.R. Hasanov, R.K. Qaimova, A.Z. Panahov, A.I. Demirel.* Ultrahigh Frequency Generation in Ga-As- type. *Studies Theor Phys.*, Vol 3, №8 293-298, 2009.
2. *E.R.Hasanov, Rasoul Nezhad Hosseyn, A.Z.Panahov and Ali Ihsan Demirel.* “Instability in Semiconductors with Deep Traps in the Presence of Strong $(\mu_{\pm} H \gg C)$ ”, *Advanced Studies in Theoretical Physics*, Vol.5, N1, p. 25-30, 2011.
3. *M.I. Iglizin, E.G. Pel, L.Y. Pervova, V.I. Fistul.* The instability of semiconductor electron-hole plazma caused by non-linearity of volt-ampere characteristics, *SSPh*, vol.8, №12, pp. 3606, 1966.
4. *E.R. Hasanov, R.A. Hasanova.* “External and internal instability in the medium having electron type conductivity», *IOSR Journal of Applied Physics*, Volume 10, Issue 3 Ver. II p. 18-26; May-June, 2018.
5. *F.F.Aliev, E.R.Hasanov.* “Nonlinear Oscillations of the charge the Carriers Concentration and Electric Field in Semiconductors with Deep Traps”, *IOSR Journal of Applied Physics*, Volume 10, Issue 1 Ver. II pp. 36-42, Jan.-Feb., 2018.
6. *E.R.Gasanov, L.E.Gurevich.* “The spontaneous current oscillations in semiconductors with deep traps in strong electric and magnetic fields”, *SSPh*. vol. 11, №12, pp. 3544-3548, 1969.
7. *E.Konuel.* The kinetic properties of semiconductors in strong electric fields, “Mir”, Moscow, pp. 339-344, 1970.
8. *A.I.Demirel, A.Z.Panahov, E.R.Hasanov.* Radiations of electron –type conductivity environments in electric and magnetic field, *Advanced Studies in Theoretical Physics*, vol.8, N22, pp. 1077-1086, 2013.

Received: 24.04.2019

TRANSPORT PROPERTIES OF SOLID SOLUTION $(\text{AgSbTe}_2)_{0.8}(\text{PbTe})_{0.2}$ S.S. RAGIMOV^{1,3}, M.A. MUSAYEV², N.N. HASHIMOVA²¹*Baku State University, Institute for Physical Problems, Baku, Azerbaijan*²*Azerbaijan State University of Oil and Industry, Baku, Azerbaijan*³*G.M. Abdullayev Institute of Physics of Azerbaijan NAS, Baku, Azerbaijan**e-mail: sadiyar@mail.ru*

The temperature dependences of the electrical conductivity and thermal power $(\text{AgSbTe}_2)_{0.8}(\text{PbTe})_{0.2}$ have been studied in the temperature range of 80-550 K. The temperature dependence of the electrical conductivity passes through a maximum in the region of 200K. A sharp jump in the temperature dependence of the thermal power in the region of 400 K was also found. The X-ray structural analysis show, that $(\text{AgSbTe}_2)_{0.8}(\text{PbTe})_{0.2}$ has a face-centered cubic structure with a lattice constant $a=6.1390\text{\AA}$

Keywords: thermoelectric material, thermal power, electrical conductivity, crystal structure**PACS:** 72.20.Pa, 74.25.F**1. INTRODUCTION**

AgSbTe_2 is a promising p-type thermoelectric material operating in the middle temperature range. Deviation from stoichiometry and the introduction of impurities are widely used in the study of AgSbTe_2 , since this makes it possible to find more suitable compositions for practical application [1-3]. One of the most attractive thermoelectric materials is AgPbmSbTe_{2+m} , which can be considered as a combination of PbTe and AgSbTe_2 in the form $(\text{AgSbTe}_2)(\text{PbTe})_m$. These compounds are called LAST-*m* (lead antimony silver telluride). LAST-*m* compounds have several distinctive properties, which make these compounds attractive. First, both AgSbTe_2 and PbTe crystallize in the structure of the cubic lattice, which allows obtaining a series of solid solutions. For LAST-*m* compositions, Vegard's law is satisfied depending on the lattice constant-composition. On the other hand, these compounds have an unusually low thermal conductivity of the lattice. Finally, LAST-*m* materials are thermally stable until they melt (<1200 K) [4].

Note that the study of $(\text{AgSbTe}_2)_x(\text{PbTe})_{1-x}$ compositions is also interesting in that both AgSbTe_2 and PbTe crystallize in the structure of the cubic

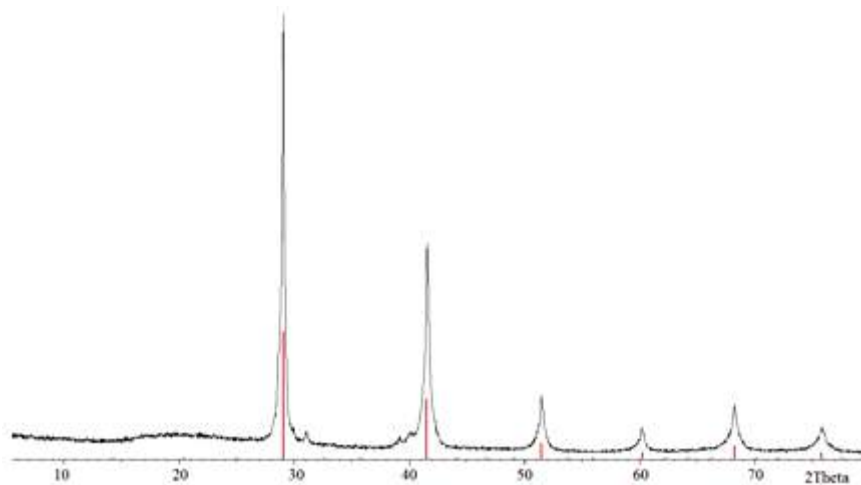
lattice, which allows obtaining a series of solid solutions. And this makes it possible to obtain compositions with different concentrations, which affects the electrical properties.

This paper presents the results of the study of structural and transport properties $(\text{AgSbTe}_2)_{0.8}(\text{PbTe})_{0.2}$ in the temperature range of 80-550 K.

2. EXPERIMENTAL RESULTS AND DISCUSSION

The studied samples were obtained by fusing the initial components in sealed quartz ampoules with an exposure of 10 hours to 100 K above the melting point with further slow cooling at a rate of 1 K/min. to room temperature.

The obtained results of X-ray diffraction analysis of $(\text{AgSbTe}_2)_{0.8}(\text{PbTe})_{0.2}$ are shown in fig. 1. X-ray diffraction analysis was performed on a BRUCKER-D2 PHASER diffractometer. According to the results of X-ray structural analysis $(\text{AgSbTe}_2)_{0.8}(\text{PbTe})_{0.2}$, it has a face-centered cubic lattice with a lattice constant $a=6.1390\text{\AA}$, and corresponds to the space group $Fm\bar{3}m$.

Fig. 1. The X-ray diffractogram of $(\text{AgSbTe}_2)_{0.8}(\text{PbTe})_{0.2}$

Electrical measurements were carried out by the four-probe potentiometric method in the temperature range of 80–550K. Potential contacts were deposited with indium. Temperature and temperature gradient were controlled by copper-constantan thermocouples. The sign of the thermal power over the entire temperature range studied is positive, which indicates a hole conduction mechanism. According to the measurements of the Hall effect, the concentration of charge carriers of $(\text{AgSbTe}_2)_{0.8}(\text{PbTe})_{0.2}$ was $p = 3.7 \cdot 10^{18} \text{ cm}^{-3}$.

The temperature dependences of the resistivity and thermal power of the investigated sample are shown in fig. 2 and fig. 3, respectively.

It was found that the temperature dependence of the electrical conductivity passes through a maximum in the region of 200K. Further, in the temperature range 200–400K, the value of electrical conductivity decreases. However, in the region of 400K, the value of electrical conductivity decreases sharply, then passing through the minimum begins to grow.

Three areas can be distinguished in the temperature dependence of the thermal power: *a*) the constancy of the thermal power value in the region of 100–300 K; *b*) an increase in the thermal power value in the temperature ranges 300–400K and above 450K; *c*) a sharp jump in the temperature dependence of the thermal power in the region of 400K. A comprehensive analysis of the transport properties suggests that acceptor levels are located near the ceiling of the valence band. Electron capture at these levels leads to an increase in the concentration of holes, as a result of which the value of electrical conductivity increases (temperature range up to 200K). Further, in a rather wide temperature range of 200–400K, strong scattering of charge carriers on acoustic phonons takes place, as a result of which the value of electrical conductivity decreases with increasing temperature. A sharp jump in the temperature dependences of the thermal power and electrical conductivity at 400K is due to the presence of the second phase Ag_2Te .

The ternary compound AgSbTe_2 crystallizes in a face-centered cubic structure of the NaCl type, in which the Ag and Sb atoms are disordered in the places of Na. At the same time, both $\text{Ag}^+ - \text{Ag}^+$ atoms and $\text{Sb}^{3+} - \text{Sb}^{3+}$ atoms can be located adjacent to each other. Energetically more beneficial are the $\text{Ag}^+ - \text{Sb}^{3+}$ location. According to [5], AgSbTe_2 contains regions ordered and disordered by Ag and Sb atoms. Such structural disorder can lead to precipitation of the

Ag_2Te phases, which strongly influences the temperature dependences of transport coefficients.

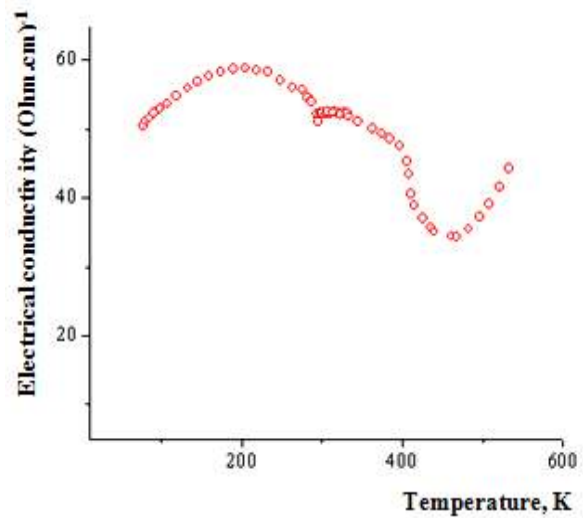


Fig. 2. The temperature dependences of the resistivity of $(\text{AgSbTe}_2)_{0.8}(\text{PbTe})_{0.2}$

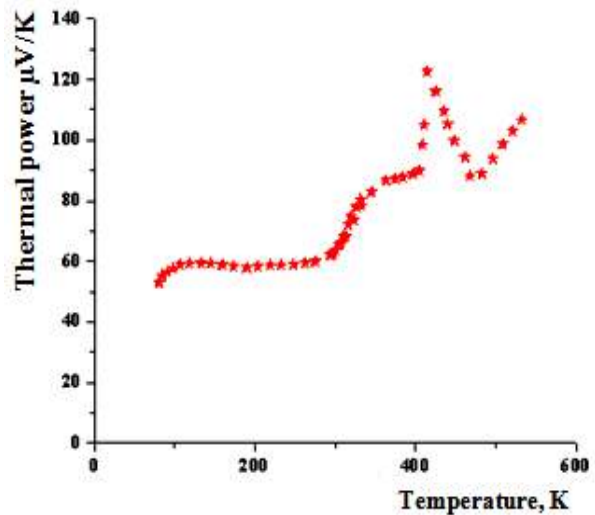


Fig. 3. The temperature dependences of the thermal power of $(\text{AgSbTe}_2)_{0.8}(\text{PbTe})_{0.2}$

3. CONCLUSION

A sharp jump in the temperature dependences of the thermal power and electrical conductivity at 400K is due to the presence of the second phase of Ag_2Te , due to the energetically more favorable arrangement of $\text{Ag}^+ - \text{Sb}^{3+}$ atoms with temperature.

- [1] A.V.Dmitriev, I.P.Zavyagin, UFN, v.180, №8, 821–838, 2010 (in Russian).
- [2] S.S. Ragimov, S.A. Aliyev. Inorganic Materials, v.43, pp. 1321–1323, 2007 (in Russian).
- [3] S.N. Guin, A. Chatterjee, K. Biswas. The Royal Society of Chemistry Adv., 4, 11811–11815, 2014.

- [4] K.F.Hsu, S.Loo, F.Guo, W.Chen, J.S.Dyck, C.Uher, T.Hogan, E.K.Polychroniadis, M.G.Kanatzidis. Science, 303, 818, 2004.
- [5] D.T.Morelli, V.Jovovic and J.P.Heremans. Physical Review Letters. №101. p. 035901, 2008.

Received: 30.04.2019

PHOTOSENSITIVITY FEATURES OF ELECTROPHOTOGRAPHIC LAYERS OF CdInGaS₄

V.G. AGAYEV

G.M. Abdullayev Institute of Physics of Azerbaijan NAS

131, H. Javid ave., Baku, AZ 1143

The quantum yield of CdInGaS₄ electrographical layers without Au impurity and with it in region (300 – 1000nm) is investigated, as result of which the photosensitivity and quantum yield in spectrum visible part increase.

Keywords: photographic materials, electrophotographic layer, layered semiconductor

PACS: 68.20; 72.20

The compounds of Aⁿ B^{vi}, Aⁿ B₂ⁱⁱⁱ C₄^{vi} [4-7] type and others from which CdInGaS₄ is considered in the present work in electrophotography (EPh) along with chalcogenide glasses [1-3]. Their monocrystalline samples are grown by us by gas-transport method. They have p-type conduction with $E_g = 2,56$ eV. At room temperature they have dark resistivity 10^{10} Ohm·cm and relative photosensitivity $\geq 10^5$ at 10^3 lux. The photosensitivity increases with Au impurity: $\geq 5 \cdot 10^6$.

The maximum of intrinsic photosensitivity is at 460nm on curves of photocurrent spectral distribution and additional maximum at Au impurity appears at 590nm. The absorption edge corresponds to 470 nm.

The investigation of absolute quantum yield of internal photoeffect of EPh layers on CdInGaS₄ base in spectrum region (300 – 1000nm).

The measurement of quantum yield in the substances with low mobility is carried out by the one of two methods: method of transient photoconduction and EPh method. The one of the main advantages of EPh method is the possibility of high field formation (of order 10^6 V·cm⁻¹) whereas the samples with metallic electrodes begin to degrade at fields $1,5 \cdot 10^5$ V·cm⁻¹ and lower than this value.

The ion contact forms at measurement in EPh mode on layer surface situated on conducting substrate. The investigation task in layers with electric charge marked on their surface is unweighted because of the strong electric field presence the discharge photocurrent achieves the saturation value and this fact allows us to easily define the quantum output of internal photoeffect.

The penetration depth of surface charge field marked on the semiconductor layer with low conductivity can be equal to significant part of layer thickness and even whole layer thickness. In the case of field penetration to the whole layer thickness the free carriers are eliminated from the layer and the charge for the surface charge compensation accumulates in the substrate. In this case the layer behavior is well described by the model of double electric layer of constant thickness (plane capacitor). Analogically this layer can be considered in the case of incomplete penetration of surface charge field introducing the thickness formed at electrification of barrier layer (effective thickness) instead of the

geometric one. We can easily ascertain calculating the capacitance of formed barrier layer $C = \frac{d\delta}{d|V|}$, where $\delta = \delta(x)$ is space charge density, $V = V(x)$ is layer potential. The potential distribution as charge functions is given by Poisson equation which has the form in one- D case:

$$\frac{d^2V}{dx^2} = \frac{4\pi\delta}{E} \quad (1)$$

where E is dielectric constant. Taking into consideration that electric field is equal to zero out of the barrier layer and on its boundaries $\frac{dV}{dx}\Big|_{x=0} = 0$, $\frac{dV}{dx}\Big|_{x=x_1} = 0$, and integrating (1) taking into consideration these boundary conditions we obtain $C = \frac{E}{4\pi d_{ef}}$ if one consider that volume charge density of barrier layer is defined by only immobile charges. The last expression is analogous to the expression for the capacity of plane capacitor.

If we consider EPh layer as the homogeneous semiconductor having the strongly defined conduction and valence bands, then the considerable displacement of free carriers on whole layer thickness by the surface charge field leads to the band bend which distributes on whole layer thickness and forms the potential barrier between surface and screening charges. The barrier appearance plays the important role on layer dark characteristics increasing on 2-3 orders the layer resistance. The surface charge sign influences on potential relaxation time and the layer thickness efficiency, i.e. on value of limiting potential. However, the photocarriers don't overcome this barrier, as the photoinjection of electron-hole pairs takes place inside the barrier. The pairs are rapidly divided by barrier strong field which has the value of $3 \cdot 10^5$ V/cm order. The carriers of one sign drift to surface charges and neutralize them and carriers of other sign pass through the layer up to approaching screening charges and also neutralize them.

The quantum yield of photogeneration of charge carriers η is determined as the ratio of Δn charge number generated by the light in the layer to ΔN number of absorbed light quanta. At layer lighting

by monochromatic light ΔV surface potential decay is expressed by the formula $\Delta V = \frac{\Delta n \cdot e}{c}$. From here

$$\eta\lambda = \frac{\Delta n}{\Delta N} = \frac{\Delta V \cdot c}{e \cdot \Delta N} \quad (2)$$

where c is layer capacitance, e is elementary charge.

Knowing ΔV , c , e and ΔN one can calculate the spectral distribution of quantum yield η_λ by the formula (2).

EPh layers are prepared by dispersion of CdInGaS₄ crystal powder in polymer binder and by deposition of obtained suspension on metallic substrates. Before the fixing in sprinkling installation these substrates are unoled by solvents, etched and preserved in acetone. The thickness of obtained layers is 20-40 μm and their main properties are study on electrometric installation with vibrating electrode near layer surface. The layer charging is carried out in corona discharge. The layer light characteristics are measured at exposure through shutter with the use of incandescent lamp and neutral filters. The source of monochromatic light is graduated by radiation compensated thermoelement PTH-30.

The layers at both polarities charge up to initial potential (600-700V) with its dark half-decay (1-2 min) at optimization of doping, thermotreatment, powder dispersion of photosemiconductor and its weight concentration. CdInGaS₄ layers with Au impurity have the value of integral sensitivity 0,4-0,9 $\text{lux}^{-1} \cdot \text{sec}^{-1}$ with low residual potential ≤ 30 V. In these layers the spectral sensitivity defined by the formula $S_\lambda = \left(\frac{1}{L_\lambda \cdot t} \right)_{\Delta V = \frac{1}{V} = \frac{1}{2}}$, $\text{cm}^2 \cdot \text{J}^{-1}$ covers

all spectrum visible part.

The layer quantum yield on base of CdInGaS₄ in the binder without Au impurity and with it calculated by formula (2) is shown in fig. 1. In the layers from undoped photosemiconductor the quantum yield rapidly increases as the quantum energy becomes enough for formation of electron-hole pairs and it is equal to $\sim 0,85$ almost up to 500nm.

At further increase of wave length the quantum yield decreases because of non photoactive radiation

absorption of layer binder material (fig.1 a). The sensitivity in sensitization absorption band appears in CdInGaS₄ layers with Au impurity and value of quantum yield achieves 1 and covers the wide region in spectrum visible part (fig. 1 b).

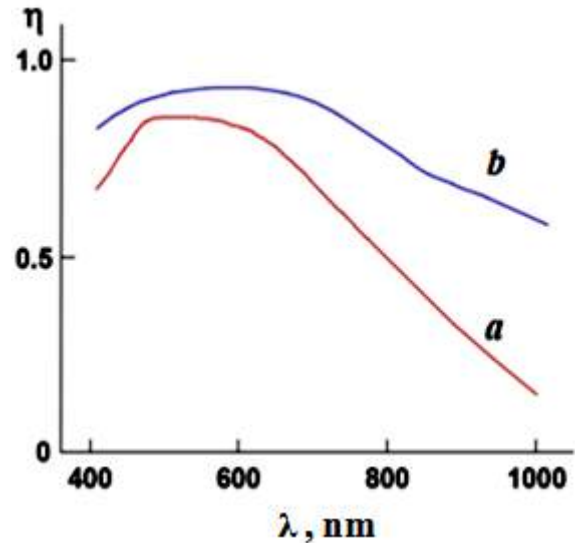


Fig.1. The spectral distribution of EPh layer quantum yield on CdInGaS₄ base without Au impurity (a) and with it (b).

We showed earlier [8-10] that the complex of photosensitivity phenomena the results of which gives the possibility to show the character of electron transitions in scheme form with three types of local centers (r and S are recombination centers and t is attachment level) in forbidden band, is observed in several crystals of A^{II}B^{III}C₄^{VI} class including CdInGaS₄. Because of big difference of cross-section values of electron and hole capture r are centers being sensory centers: they rapidly capture non-main carriers and slowly capture the main ones that leads to strong monopolarity and high values of photosensitivity.

- [1] N.I. Ibragimov, V.G. Agayev, Z.M. Abutalibova. The certificate of authorship of USSR: № 1568016, 1990; №1675837, 1991; № 1730608, 1992; № 1807442, 1992 (in Russian).
- [2] N.I. Ibragimov, V.G. Agayev, Z.M. Abutalibova. Thin Solid Films, v. 196, p. L1, 1991.
- [3] N.I. Ibragimov, Z.M. Abutalibova, V.G. Agayev. Thin Solid Films, v. 359, p. 125, 2000.
- [4] G.B. Abdullayev, V.G. Agayev and others. The certificate of authorship of USSR: №467315, 1974; №560200, 1977; №627707, 1978; №1301169, 1986; №1301169, 1986; №1403010, 1988; № 1603335, 1990.
- [5] V.G. Agayev, N.I. Ibragimov. Fizika, v. 7, № 2, p.32, 2001.
- [6] V.G. Agayev, N.I. Ibragimov. Fizika, v. 9, № (3, 4), p. 41, 2003.
- [7] V.A. Agayev, Fizika, vol.13, № 4, p.102, 2007.
- [8] G.B. Abdullayev, V.G. Agayev, G.X. Nani, E.U. Salayev. Semiconductors, v.6, № 9, p.37, 1972.
- [9] G.B. Abdullayev, V.G. Agayev, G.X. Nani, E.U. Salayev, Semiconductors, v.11, № 1, p.14, 1977.

Received: 13.05.2019

DEPENDENCE OF ELECTRON MOBILITY ON THEIR SURFACE DENSITY IN A SEMICONDUCTOR QUANTUM WELL WITH THE MODIFIED PÖSCHL -TELLER CONFINING POTENTIAL

M.M. BABAYEV, X.B. SULTANOVA, M.Q. ABBASLI

G.M.Abdullayev Institute of Physics of Azerbaijan NAS

131, H. Javid ave., Baku, AZ 1143

e-mail: mirbababayev@yahoo.com

The dependence of electron mobility on their surface density in a semiconductor quantum well is studied. The modified Poschl-Teller potential is used as the confining potential in the quantum well. It is shown that the dependence of electron mobility on their surface density is close to linear. Comparison of the obtained theoretical results with experimental data shows that the modified Poschl-Teller potential represents the confining potential in $GaAs/Al_xGa_{1-x}As$ quantum well properly.

Keywords: quantum well, Poschl-Teller potential, mobility.

PACS: 73.63.-b; 73.63.Hs

Semiconductor quantum well is the quantum film in which the motion of the charge carriers is not restricted in two directions (let us assume the Cartesian coordinates in these directions x and y) but in one direction (the z -axis). Theoretical study of transport phenomena in electron gas in semiconductor quantum wells requires to choose the shape of the confining potential in the z -direction. Since the actual shape of this potential is unknown [1], different models are used in theoretical researches. In scientific literature, the most used models are the square well potential [1] and the parabolic well potential [2]. In real crystals the energy of electrons depends on z and height of potential is finite quantity. The flaw of square well potential is that this model does not consider z dependence; parabolic model considers this dependence but its value tends to infinity at large distances.

In recent years the modified Poschl-Teller potential has been used as the confining potential in quantum wells [3-5]. This potential has a shape between square well and parabolic well models, depends on z and gets finite value at large z (fig. 1).

In the present paper dependence of the mobility of electrons on their surface density in a quantum well with the modified Poschl-Teller potential is studied. This potential can be written as [6]:

$$U(z) = \frac{\hbar^2 \alpha^2}{2m} \lambda(\lambda + 1) \tanh^2 \alpha z, \lambda > 0 \quad (1)$$

Since in x and y directions motion is not restricted, dispersion law of electrons with potential (1) is as follows:

$$\varepsilon(k_x, k_y) = E_{\lambda, N} + \frac{\hbar^2 (k_x^2 + k_y^2)}{2m}$$

$$E_{\lambda, N} = \frac{\hbar^2 \alpha^2}{2m} [\lambda(\lambda + 1) - (N - \lambda)^2] \quad (2)$$

Here m is the effective mass of conduction electrons, k_x and k_y are the projections of wave vector of electrons, respectively in x and y directions, $N=0,1,2, \dots$ is the number of energy levels ($N \leq \lambda$).

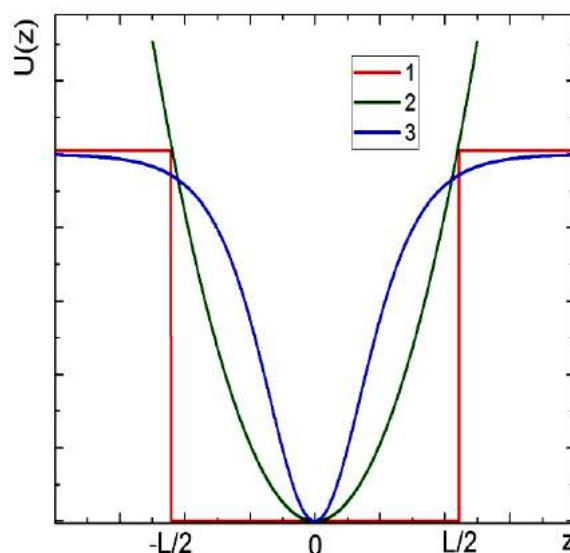


Fig. 1. Different models of confining potential: 1- square well, 2- parabolic, 3- modified Poschl-Teller potential (L - width of the quantum well).

Wave function of the electrons with energy spectrum (2) is given as:

$$\psi_{N, \lambda, k_x, k_y}(\vec{r}) = \frac{e^{i(k_x x + k_y y)}}{\sqrt{L_x L_y L_z}} \left[\frac{\alpha(\lambda-1)\Gamma(2\lambda-N+1)}{N!} \right]^{\frac{1}{2}} P_{\lambda}^{N-\lambda}(\tanh \alpha z) \quad (3)$$

Here $\vec{r}(x, y, z)$ – coordinates of the electron, L_x, L_y, L_z – dimensions of the sample in the respective directions, $P_\lambda^{N-\lambda}(\tanh \alpha z)$ are the Legendre functions [6].

The analysis of the results of most experiments performed in quantum films shows that electrons occupy the states with the lowest energy ($N = 0$), namely the average energy satisfies the relation $\bar{\epsilon} < \hbar^2 \alpha^2 / 2m$. So we can take parameters of the potential as $\lambda = 1, N = 0$.

Let us assume the case that the electric field is directed along the quantum film. Then in order to find the mobility, Boltzmann kinetic equation can be used. We are going to use the relaxation time approximation. In the absence of magnetic field and temperature gradient the distribution function of electrons can be written as follows [7]:

$$f(k_x, k_y) = f_0(\epsilon) + \frac{e}{\hbar} \tau(\epsilon) \vec{E} \nabla_{\vec{k}} f_0(\epsilon) \quad (4)$$

Here $f_0(\epsilon)$ is the isotropic part of the distribution function, \vec{E} – the intensity of the electric field, $\tau(\epsilon) = (v_{ak} + v_{pz} + v_i)^{-1}$ is the total relaxation time due to different scattering mechanisms, v_{ak}, v_{pz} , and v_i are scattering rates due to acoustic and piezoacoustic phonons and impurity ions, respectively. These rates were calculated in [4] and [5]. When the distribution function of electrons is known (4) mobility can be derived from the expression for current density along the quantum film:

$$\vec{j} = -2e \sum_{k_x, k_y} \vec{v} f(k_x, k_y) \quad (5)$$

Here $\vec{v} = \hbar \vec{k} / m$ is the electron velocity. If we take into account (4) in equation (5) and convert the summation over k_x and k_y into an integral, we get:

$$\vec{j} = \frac{e^2 \hbar^2}{2 \pi^2 m^2} \int_{-\infty}^{\infty} \left(-\frac{\partial f_0}{\partial \epsilon} \right) \tau(\epsilon) \vec{k} (\vec{k} \cdot \vec{E}) dk_x dk_y \quad (6)$$

We can write the last expression in polar coordinates (k, φ) and integrate over angle φ :

$$\vec{j} = \frac{e^2 \hbar^2}{2 \pi m^2} \vec{E} \int_0^{\infty} \left(-\frac{\partial f_0}{\partial \epsilon} \right) \tau(\epsilon) k^3 dk = \sigma \vec{E} \quad (7)$$

Here σ is conductivity. When electrons are located in parabola with the lowest energy ($N=0$) for the chemical potential of electrons we get:

$$\zeta = \frac{\hbar^2 \alpha^2}{2m} + k_0 T \ln \left[\exp \left(\frac{\pi \hbar^2 n}{m k_0 T} \right) - 1 \right] \quad (8)$$

Here k_0 – Boltzmann constant, T – the temperature of the crystal, n – the surface density of electrons. Note that $E_{l,0} = (\hbar^2 \alpha^2 / 2m)$ is the minimum of the parabola with the lowest energy. Let us take origin as the minimum of the parabola and consider new variables as below:

$$x = \frac{\epsilon}{k_0 T} - \frac{\hbar^2 \alpha^2}{2m k_0 T} = \frac{\hbar^2 k^2}{2m k_0 T}, \quad \eta = \frac{\zeta}{k_0 T} - \frac{\hbar^2 \alpha^2}{2m k_0 T} \quad (9)$$

Then electron mobility $\mu = \sigma / ne$ can be written as:

$$\mu = \frac{e k_0 T}{\pi \hbar^2 n} \int_0^{\infty} \frac{e^{x-\eta}}{(e^{x-\eta} + 1)^2} \tau(x) x dx \quad (10)$$

At low temperatures, the main mechanism of the scattering is the scattering by impurity ions. In this case mobility of electrons becomes:

$$\mu = \frac{\chi^2 (k_0 T)^2}{2 \pi^2 \hbar e^3 \alpha^2 n n_i} \int_0^{\infty} \frac{e^{x-\eta}}{(1 + e^{x-\eta})^2} \left[\int_0^1 \frac{I^2(k, t) dt}{\epsilon^2(k, t) \sqrt{1-t^2}} \right]^{-1} x^2 dx \quad (11)$$

$$\text{Here, } k = (\sqrt{2 m k_0 T / \hbar}) x^{1/2}, I(k, t) = \int_0^{\infty} e^{-2kzt} (1 - \text{Tanh}[\alpha z]^2) dz, t = \frac{q}{2k}.$$

χ – the static permittivity, n_i – surface density of ions in the quantum well, $q = |\vec{k}_2 - \vec{k}_1|$ – the magnitude of the difference of two-dimensional wave vectors of the interacting electrons, $\epsilon(k, t)$ is dielectric function [4,5]:

$$\epsilon(q) = 1 + \frac{2m e^2}{\hbar^2 \chi q} \left\{ \frac{1}{2} \left(\frac{q}{\alpha} \right)^2 \Psi^{(1)} \left(-1 + \frac{q}{2\alpha} \right) - \frac{4 + \left(\frac{q}{\alpha} - 1 \right) \left(\frac{q}{\alpha} \right)^2}{\left(\frac{q}{\alpha} - 2 \right)^2} \right\} f_0 \left(\frac{\hbar^2 \alpha^2}{2m} \right) \quad (12)$$

Here $\Psi^{(1)}(z) = \frac{d^2}{dz^2} \ln \Gamma(z)$ – trigamma function, $\Gamma(z)$ – gamma function, $f_0 \left(\frac{\hbar^2 \alpha^2}{2m} \right)$ – occupation probability of the lowest energy state ($k = 0$).

From (11) dependences of mobility on the temperature, the surface density of impurity ions and electrons can be investigated. In quantum wells dependence of the mobility of electrons on their surface density is sharply different from the bulk

crystals. The reason is that in bulk impurity semiconductors concentrations of electrons and ions have the same order of magnitude, while in the quantum film it is possible to increase the surface density of electrons compared to surface ion density sufficiently. For example, in heterostructure $\text{Al}_x\text{Ga}_{1-x}\text{As}/\text{GaAs}$ number of electrons in quantum well (GaAs) increases by one or two orders of magnitude because of the electrons coming from the environment ($\text{Al}_x\text{Ga}_{1-x}\text{As}$) [8,9]. Since the ions in the $\text{Al}_x\text{Ga}_{1-x}\text{As}$ part of the heterostructure are far from the electrons in

GaAs quantum well, their influence on scattering of electrons is insignificant, consequently increasing of surface density of electrons causes significant increase of mobility.

Let us compare obtained theoretical results with experimental ones [8] in n -type GaAs/ $\text{Al}_x\text{Ga}_{1-x}\text{As}$ quantum well. In this experiment, the electron mobility is measured in the interval of the surface density of electrons $n = (1 \div 8) \cdot 10^{15} \text{ m}^{-2}$. At these values of electron surface density at low temperatures ($T < 20\text{K}$) electrons are strongly degenerate, then η (reduced chemical potential) and k can be written as $\eta = 2\pi\hbar n / mk_0 T$ and $k = \sqrt{2\pi n}$, respectively.

Let us calculate mobility numerically at $T = 12 \text{ K}$ in which experiment is performed. Values of used parameters [10]: $m = 0.067m_0$ (here m_0 – free electron mass), $\rho = 5.3 \cdot 10^3 \text{ kg/m}^3$, $\chi = 12.9$, $E_I = 7.4 \text{ eV}$, $e_{14} = 0.16 \text{ C/m}^2$.

In order to find parameter α of the modified Poschl-Teller potential we use the fact that the factor before $\tanh^2 \alpha z$ function (1) is equivalent to the depth Δ of the quantum well [5]; when $\lambda = 1$:

$$\frac{\hbar^2 \alpha^2}{m} = \Delta \quad (13)$$

In the experiment [8] the proportion of GaAs in $\text{Al}_x\text{Ga}_{1-x}\text{As}$ film is $x = 0.3$. If we take into account that band gaps of the AlAs and GaAs are 2.23 eV and 1.52 eV , respectively [10], at $x = 0.3$ for the band gap of the $\text{Al}_x\text{Ga}_{1-x}\text{As}$ we get $E_g \approx 1.52(1-x) + 2.23 x \approx 1.73 \text{ eV}$. Then $\text{Al}_x\text{Ga}_{1-x}\text{As}$ and GaAs films have band gap difference of $\Delta E_g \approx 0.21 \text{ eV}$. The depth of n -type quantum well is equal to the difference of the minimums of the conduction bands in heterojunction. From scientific literature [11] it is known that this difference can approximately be found from the condition $\Delta \approx 0.7 \Delta E_g$. Then from expression (13) for the parameter of the potential, we get $\alpha \approx 3.6 \cdot 10^8 \text{ m}^{-1}$. We will use this value of α in numerical calculations.

The dependence of mobility on the electron surface density has been calculated at the different values of the surface density of the ions and given in fig. 2(a). As seen from the figure the dependence of

electron mobility on their surface density is close to linear dependence.

In fig. 2(b) the comparison of the obtained theoretical results with experimental ones [8] is given at $n_i = 6 \times 10^{14} \text{ m}^{-2}$. From this figure, we can see that obtained theoretical results fit well with experimental results. Based on this, we can conclude that the modified Poschl-Teller potential represents confining potential in GaAs/ $\text{Al}_x\text{Ga}_{1-x}\text{As}$ quantum well properly.

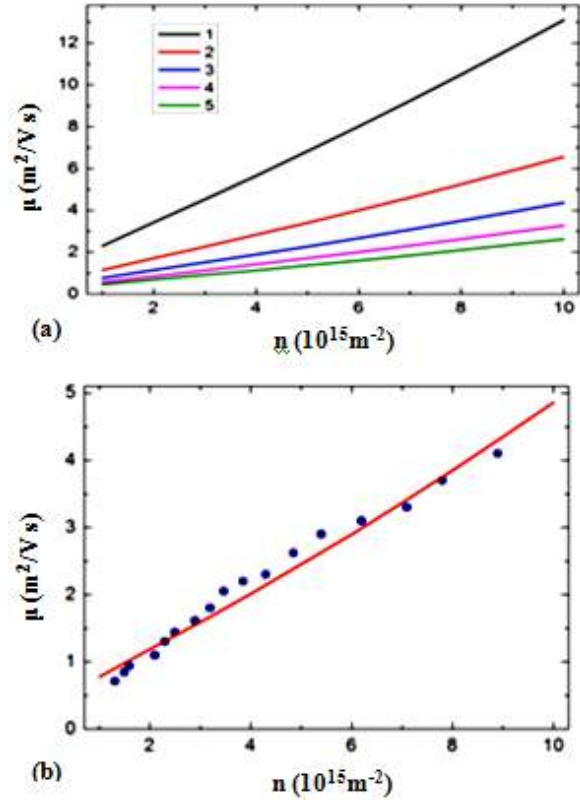


Fig. 2. (a) Dependence of electron mobility on their surface density at: 1- $n_i = 2 \times 10^{14} \text{ m}^{-2}$; 2- $n_i = 4 \times 10^{14} \text{ m}^{-2}$; 3- $n_i = 6 \times 10^{14} \text{ m}^{-2}$; 4- $n_i = 8 \times 10^{14} \text{ m}^{-2}$; 5- $n_i = 10^{15} \text{ m}^{-2}$; (b) Comparison of experimental and theoretical results at $n_i = 6 \times 10^{14} \text{ m}^{-2}$; line - theoretical, dots - experimental results.

- [1] T.Ando, A.B.Fowler, F.Stern, Rev. Mod. Phys., 54, 1982, 437.
- [2] F.M. Hashimzade, Kh.A. Hasanov, M.M. Babayev. Phys. Rev. B, 73, 235349, 2006.
- [3] P.P.Kostrobyi, I.A.Ryzha. Journal of National University "Lvivska Politechnika", Phys. Math. Sci., 718, 89, 2011.
- [4] M.M.Babayev, X.B.Sultanova, N.B.Mustafayev, AJP Fizika, XXII, 19, 2016.
- [5] M.M.Babayev, Kh.B.Sultanova, N.B. Mustafayev. Chinese J. Phys., 56, 2977, 2018.
- [6] S.Cruz y Cruz, S. Kuru, J. Negro, Phys. Lett. A, 372, 1391, 2008.
- [7] B.M. Askerov. The electron phenomena of transfer in semiconductors. Moscow, Science, p.318, 1985.
- [8] K. Hirakawa and H. Sakaki, Phys. Rev. B, 33, 8291, 1986.
- [9] R.Fletcher, J.C.Maan, G.Weimann. Phys. Rev. B, 32, 8477, 1985.
- [10] V.F.Gantmakher, V.B.Levinson. Carrier Scattering in Metals and Semiconductors, North-Holland, Amsterdam, 1987.
- [11] S.V. Evstigneyev, R.M. Imamov, A.A. Lomov, U.G. Sadofyev, U.V. Khavarov, M.A. Chuyev, D.S. Shipizhin. Semiconductors, 34, 719, 2000.

Received: 14.05.2019

PHOTOLUMINESCENCE PROPERTIES OF $\text{Ni}_{1-x}\text{Zn}_x\text{Fe}_2\text{O}_4$ NANOPOWDERS

Sh.A. AHMADOVA, T.G. NAGHIYEV, Sh.N. ALIYEVA,
A.A. SADIGOVA, T.R. MEHDIYEV

*G.M. Abdullayev Institute of Physics of Azerbaijan NAS,
131, H. Javid ave., Baku, AZ 1143*

The photoluminescence spectra of $\text{Ni}_{1-x}\text{Zn}_x\text{Fe}_2\text{O}_4$ ferrite nanopowders with different Zn contents were studied. The experiments were carried out at 300K, spectral lines were used to excitation luminescence: Xe-lamp with the wavelength 280 nm, 290 nm, 300 nm, 325 nm, 350 nm, 375 nm, 388 nm, 400 nm, 425 nm, and also YAG Nd laser ($\lambda = 532$ nm). The obtained spectra were interpreted in the framework of the proposed model in [1] for Fe_3O_4 , a structural analogue of $\text{Ni}_{1-x}\text{Zn}_x\text{Fe}_2\text{O}_4$ ferrites.

Keywords: ferrites, photoluminescence, nanopowders, sublattice

PACS: 41.20 Gz; 42.72 Ai

1. INTRODUCTION

In this study, the results of experimental investigations of the effect of magnetic inhomogeneity on the luminescence spectra of $\text{Ni}_{1-x}\text{Zn}_x\text{Fe}_2\text{O}_4$ ferrite nanopowders with different concentrations of Ni and Zn. It is known that $\text{Ni}_{1-x}\text{Zn}_x\text{Fe}_2\text{O}_4$ ferrites are still of great scientific interest because of the high practical relevance, as shown by an unrelenting amount of scientific publications. The characteristic features of these ferrites [2] is the presence of two magnetic sublattices bound by indirect exchange interaction (the dipole interactions between the atoms of each of the sublattices are much smaller than the exchange interaction between the atoms of different sublattices). Another feature of the studied ferrite compositions is a gradual (with the concentration of zinc) conversion of the inversed spinel structure into the normal spinel structure without changing symmetry, but there is a transition from the ferromagnetic to antiferromagnetic ordering. It is known that nickel-zinc ferrites having a spinel structure are widely used in the field of modern radio engineering, nanoelectronics, automation, data processing and transmission systems, and also for the development of various functional elements. Therefore, obtaining these materials and studying their optical properties in a wide range of wavelengths is of scientific interest. The studies of Mössbauer [3, 4] spectra showed that there is a weak magnetic phase [5] in nanopowders of magnetite a structural analogue of $\text{Ni}_{1-x}\text{Zn}_x\text{Fe}_2\text{O}_4$ ferrites with the grain size about from 15 to 45 nm. The parameters of this phase could not be determined because of the low intensity of the respective peaks and impossibility of their separation from the intense peaks of iron ions of the A and B sublattices. Therefore, the weak magnetic sublattice parameters are not defined.

From this point of view, the main purpose of studying the photoluminescence processes of $\text{Ni}_{1-x}\text{Zn}_x\text{Fe}_2\text{O}_4$ ($x=0; 0.25; 0.4; 0.5; 0.6; 0.75; 1$) excited by sources with different wavelengths is to investigate of magnetic excitations, optical properties and weak

magnetic phase parameters in the nano-powders of these materials.

2. SAMPLES PREPARATION

The $\text{Ni}_{1-x}\text{Zn}_x\text{Fe}_2\text{O}_4$ nano-powders, where $x = 0; 0.25; 0.4; 0.5; 0.6; 0.75; 1$ were synthesized by the method of high-temperature sintering of high purity NiO, ZnO and Fe_2O_3 compounds followed by annealing for 2 hours at 960°C [6]. The particle sizes of the nanopowders of all the compositions were about 20- 40 nm. The quality of nanopowders was monitored by X-ray diffractograms and optical methods. It is shown that lattice distortions resulting from deviation from stoichiometry have little effect on Raman spectra. Detailed X-ray studies of the formation of $\text{Ni}_{1-x}\text{Zn}_x\text{Fe}_2\text{O}_4$ ferrite films have shown that the process of their formation, as pointed in [7], goes through three stages: at the first stage ZnFe_2O_4 is obtained, while part of NiO and Fe_2O_3 remain in the free state; in second stage the process of including Ni^{2+} ions in the ZnFe_2O_4 lattice begins and compound with an excess of Ni content are formed against stoichiometry; in the third stage the composition compound is finally formed. All observed changes are in good agreement with changes in the content of Fe^{3+} cations [8] in the compositions of $\text{Ni}_{1-x}\text{Zn}_x\text{Fe}_2\text{O}_4$ films.

We note that it was established in [9] that the most homogeneous composition of ZnFe_2O_4 , accompanied by the largest incorporation of Fe ions into the ZnO structure, is achieved when using $\alpha\text{-Fe}_2\text{O}_3$ powders. A significantly smaller amount of Fe is included into the ZnO structure in samples obtained on the basis of FeO and Fe_3O_4 .

The spatial symmetry group of $\text{Ni}_{1-x}\text{Zn}_x\text{Fe}_2\text{O}_4$ corresponded to $Fd\bar{3}m$. However, all $\text{Ni}_{1-x}\text{Zn}_x\text{Fe}_2\text{O}_4$ ferrite compositions, except ZnFe_2O_4 , referring to normal spinel ($x = 1$), have a reverse spinel structure, a good idea of which for the NiFe_2O_4 case ($x = 0$) can be seen in fig. 1 in [10, 11, 12, 13]:

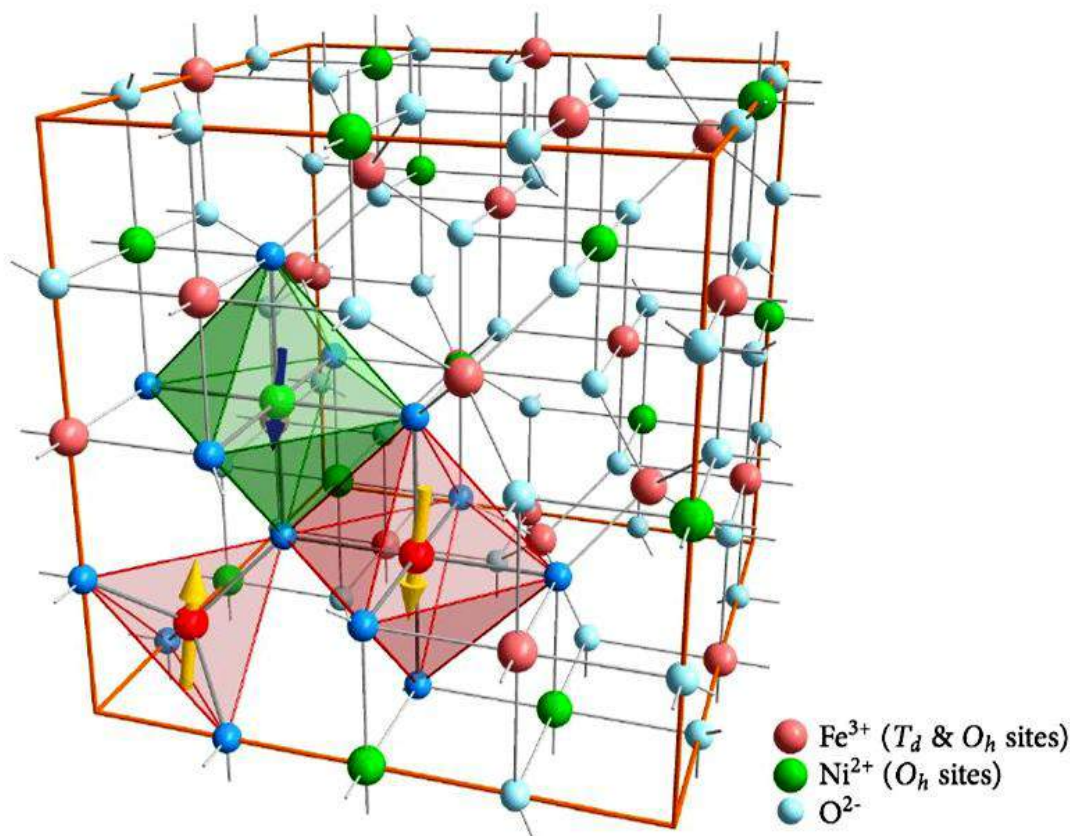


Fig.1. The unit cell of the inverse spinel lattice of NiFe_2O_4 : Fe^{3+} -cations (red) are distributed equally across tetragonal (T_d) and octahedral (O_h) lattice sites, while Ni^{2+} -cations (green) occupy O_h sites. An antiferromagnetic coupling between the T_d and O_h sites compensates the magnetic moments of the Fe^{3+} -cations, why only the Ni^{2+} -cations account for the net macroscopic magnetization of $2 \mu_B/\text{f.u}$ [10]

3. RESULTS AND DISCUSSION

3.1. EXPERIMENTAL DETAILS

The luminescence spectra of all synthesized $\text{Ni}_{1-x}\text{Zn}_x\text{Fe}_2\text{O}_4$ nano-powders compositions were studied on LS-55 spectrometer with a Monk-Giddison monochromator at room temperature in the 300-700 nm wavelength range. The following symbols were used on the fig. 3: A, B, C, etc. - luminescence spectra when excited from the Xe source: 280 nm (4.427 eV), 290 nm (4.275 eV), 300 nm (4.132 eV), 325 nm (3.814 eV), 350 nm (3.542 eV), 375 nm (3.306 eV), 388 nm (3.195 eV), 400 nm (3.099 eV), 425 nm (2.917 eV); a , b , etc. - compositions: $x = 0; 0.25; 0.4; 0.5; 0.6; 0.75; 1$ respectively. The numbers 1, 2 and etc. in table 1 denote the energies and wavelengths of electronic transitions averaged over the investigated compositions. The top lines of the table cell are nm, the bottom lines- eV.

The luminescence spectra of all synthesized $\text{Ni}_{1-x}\text{Zn}_x\text{Fe}_2\text{O}_4$ nano-powders compositions were also investigated on the Confocal Raman Spectrometer, 3D Confocal Laser Microspectroscopy System Nanofinder 30 (Tokyo Instruments, Japan). The source of excitation is the YAG Nd laser ($\lambda = 532$ nm), with the possibility of changing the radiation power from 0.1 mW to 10 mW. These studies revealed the

presence of a photoluminescence band in the region of 600-1000 nm, with a maximum at 822 nm, the intensity of which depended on the composition. The maximum band of this photoluminescence is practically independent on the power of the exciting radiation.

3.2. DISCUSSION

Ni-Zn ferrites exhibit red photoluminescence within excitation by xenon lamp radiation at 393 nm at room temperature. The emission spectrum is composed of a several groups of sharp lines in the range of about 530-710 nm with the most intensive line at 612 nm. The photoluminescence excitation spectra of emission lines at 587 nm, 612 nm and 700 nm have evidently similar structure. They are composed of broad band in the range of 250-320 nm with maximum at about 275 nm and a series of sharp lines in the range of 350-550 nm with the most intensive at 363 nm, 393 nm and 466 nm [1].

Fig. 2 shows the approximate band structures of the Fe_3O_4 nanoparticles, as estimated by our photoluminescence measurements. A near-infrared peak is observed at ~ 840 nm (1.47 eV), which can be attributed to the electron traps on the tetrahedral site, that are associated with the oxygen vacancies. Their

mutual correlation is beyond doubt, as mentioned earlier, is a consequence of the exchange processes between Fe^{3+} and Fe^{2+} ions. It should be noted that a similarity of this maximum is also performed in the photoluminescence spectra of the authors, for instance

[1, 14]. For the following interpretation of the obtained results, we used the scheme of the energy bands of the Fe_3O_4 nanoparticle systems, published in [1]:

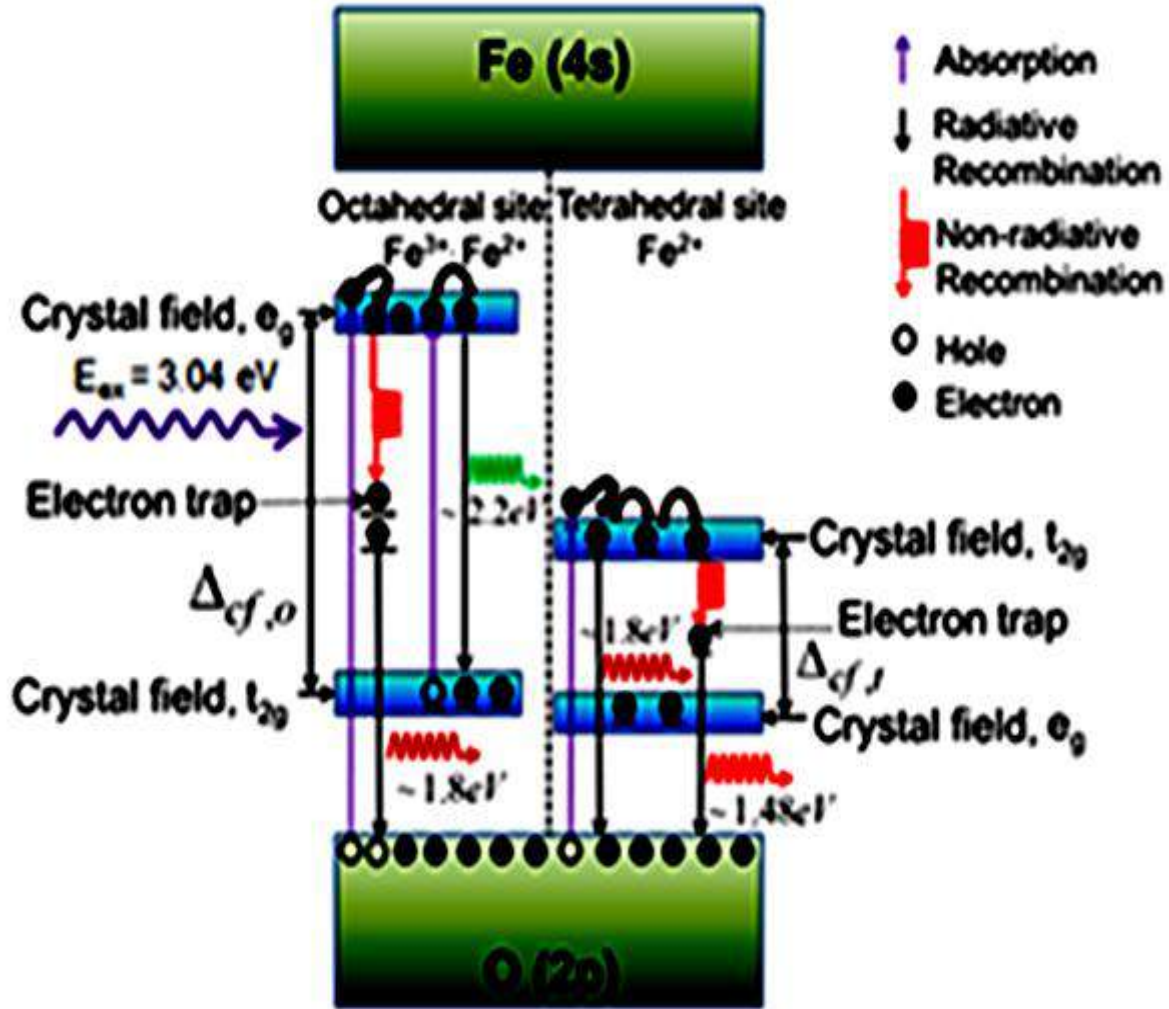


Fig. 2. The schematic of the energy bands of the Fe_3O_4 nanoparticle systems [1]

PAA- Fe_3O_4 photoluminescence measurements (PAA-hydrophilic coatings) when illuminated with 407 nm laser light (3.05 eV), published in [1], revealed three main peaks in the spectral range of 10–5000 nm: about 540 nm, 690 nm, and 840 nm. Similar photoluminescence spectra were obtained using 449 nm (2.76 eV) radiation for excitation. The photoluminescence spectra contained two main peaks: at 550 nm (2.10 eV) and 674 nm (1.84 eV) for the PAA- Fe_3O_4 samples, whereas for the Fe_3O_4 samples only one peak was observed at 674 nm (1.84 eV) [1]. In the present study, all these peaks were also observed.

According to [1], the photoluminescence peak near 550 nm (2.30 eV) is explained by the radiative recombination of mobile electrons from $t_{2g} \rightarrow e_g$ (2.2 eV) at the octahedral site. A much weaker peak at $\sim 690 \text{ nm}$ (1.79 eV) corresponds to recombination of trapped electrons from the octahedral site to O (2p) at

the tetrahedral site. In addition, from [14], it is possible to see the intensity of the emission bands at 541.94 and 518.93 nm, which changes with increasing Zn/Ni substitution. Obviously, these intensities increase with increasing Zn content, except for $x=0.5$. This can be explained as follows: 1) based on the analysis of MAUD with increasing concentration of Zn^{2+} and leaving Ni^{2+} cations in the structure, Zn^{2+} ions occupy tetrahedral sites and transfer Fe^{3+} to octahedral sites, 2) these changes lead to a decrease in the structural isotropy of the synthesized nano-crystals, with the exception of the $\text{Ni}_{0.5}\text{Zn}_{0.5}\text{Fe}_2\text{O}_4$ nano-crystals, 3) nano-crystals have the highest saturation magnetization among the synthesized nano-crystals and have structural isotropy in the tetrahedral regions, 4) the capture of half of the tetrahedral sites by Zn^{2+} ions and the rest by Fe^{3+} ions leads to a decrease in the transitions of Fe^{3+} ions in tetrahedral sites.

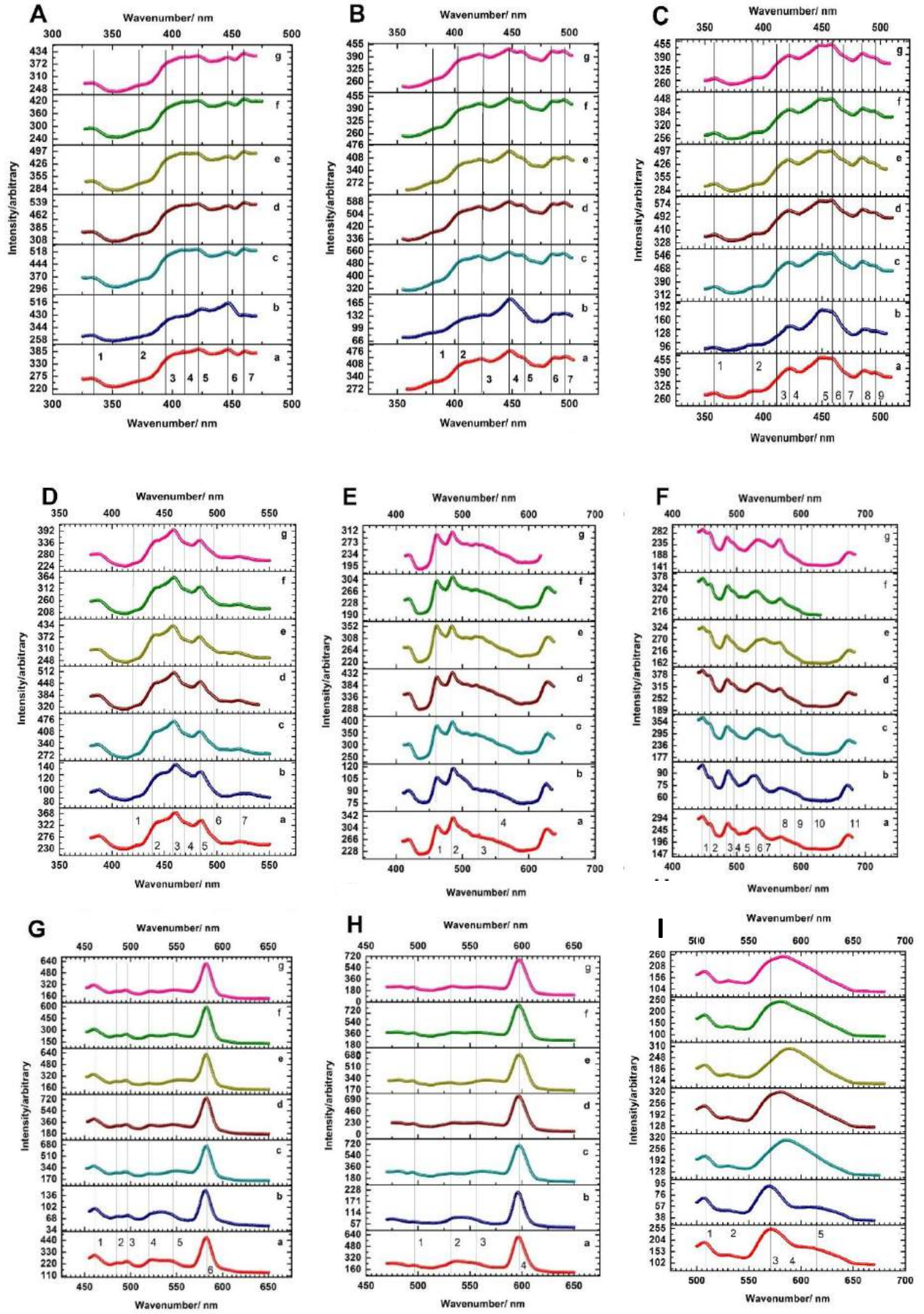


Fig. 3. Photoluminescence spectra of $\text{Ni}_{1-x}\text{Zn}_x\text{Fe}_2\text{O}_4$ nanopowders (A, B, C, D, E, F, G, H, I - luminescence spectra when excited from the Xe source: 280 nm, 290 nm, 300 nm, 325 nm, 350 nm, 375 nm, 388 nm, 400 nm, 425 nm respectively)

Table 1.

Comparison the results of [1] work and obtained from our investigation of energies and wavelengths of electronic transitions of photoluminescence spectra of $\text{Ni}_{1-x}\text{Zn}_x\text{Fe}_2\text{O}_4$ ferrite nano-powders

Experimental data [1]	-	-	-	-	-	-	-	-	-	-
407 nm 3.05 eV										
Our Investigation (nm, eV)	332 3.734	372 3.332	396 3.13	406 3.053	421 2.945	446 2.779	461 2.689	486 2.551	496 2.499	522 2.375

Experimental data [1]	540 2.3	-	-	-	-	690 1.8	840 1.47
407 nm 3.05 eV							
Our Investigation (nm, eV)	548 2.262	558 2.222	598 2.073	628 1.974	636 1.949	683 1.81	873 1.42
YAG Nd laser ($\lambda = 532$ nm)	-	-	-	-	-	682.8	873

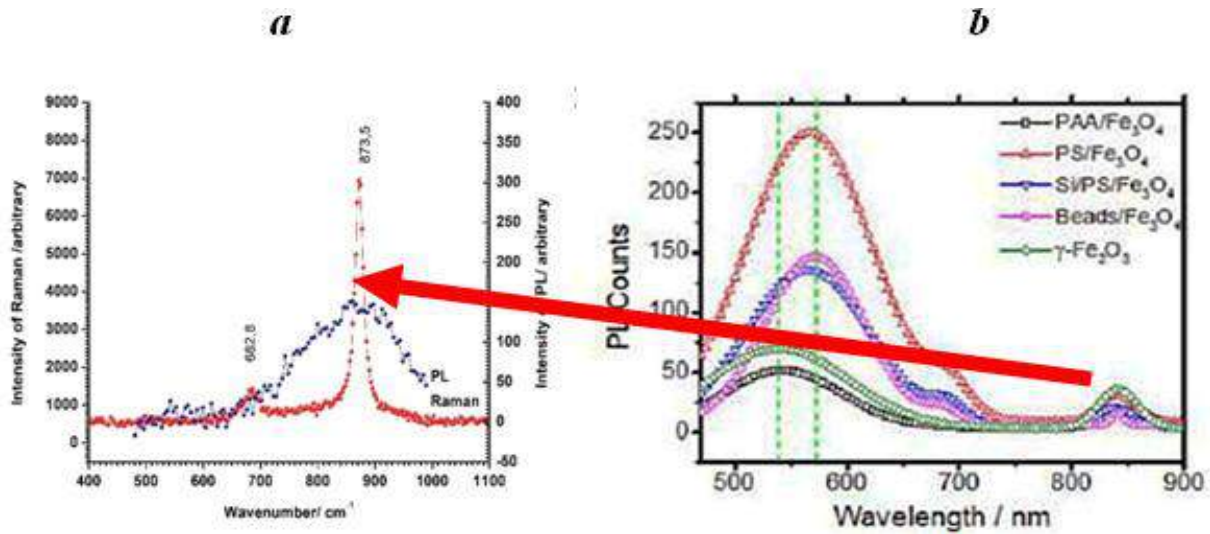


Fig.4. $\text{Ni}_{0.4}\text{Zn}_{0.6}\text{Fe}_2\text{O}_4$ thin film (a) [15] and Fe_3O_4 (b) (840cm^{-1}) [1] to the maximum of oxygen vacancies is indicated by a red arrow. The blue color indicates the components of the photoluminescence spectrum of $\text{Ni}_{0.4}\text{Zn}_{0.6}\text{Fe}_2\text{O}_4$ nanopowders, and the red color indicates a maximum of 873 cm^{-1} in the Raman spectrum of $\text{Ni}_{0.4}\text{Zn}_{0.6}\text{Fe}_2\text{O}_4$ thin films (a)

Comparing the results obtained with the known studies [1, 15], we note that, with a common similarity, they contain information on previously unrecorded electronic transitions, as well as the dynamics of the change in the luminescence spectra with a change concentration in the composition.

3. CONCLUSION

The photoluminescence spectra of $\text{Ni}_{1-x}\text{Zn}_x\text{Fe}_2\text{O}_4$ nanopowders ($x=0; 0.25; 0.4; 0.5; 0.6; 0.75; 1$) were

studied at various energies and excitation powers. The transition energies are determined and a tentative interpretation is given.

4. ACKNOWLEDGEMENT

This work was supported by the Science Development Foundation under The President of the Republic of Azerbaijan-Grant № EIF-BGM-3-BRFTF-2+/2017-15/04/1.

-
- [1] *M.E.Sadat, Masoud Kaveh Baghbador, Andrew W. Dunn, H.P. Wagner, Rodney C. Ewing, Jiaming Zhang, Hong Xu, Giovanni M. Pauletti, David B. Mast, and Donglu Shi.* Photoluminescence and photothermal effect of Fe_3O_4 nanoparticles for medical imaging and therapy, *Applied Physics Letter*, 105, 091903-1-091903-5, 2014.
 - [2] *E.W. Gorter.* Philips Res. Rep., 9, 4, 295, 5, 321, 6, 403, 1954.
 - [3] *M.Sorescu, L. Diamandescu, R. Peelamedu, R. Roy, P. Yadoji.* Structural and magnetic properties of NiZn ferrites prepared by microwave sintering, *Journal of Magnetism and Magnetic Materials*, 279 (2004), 195–201, doi:10.1016/j.jmmm., 01.079, 2004.
 - [4] *V. Blanco-Gutiérrez, M.J. Torralvo, Sáez-PucheR. and P.Bonville.* Magnetic properties of solvothermally synthesized ZnFe_2O_4 nanoparticles *Journal of Physics: Conference Series* 200,072013, 5 p., 2010.
 - [5] *V.G. Kostishyn, B.K.Ostafiyshuk, V.V.Moklyak, A.V.Nuriev.* Materials of Electronics Engineering, 2013, 4, 22-29.
 - [6] *A.A.Sadigova, S.A.Ahmadova, Sh.N.Aliyeva, T.R.Mehdiyev.* IR Diffuse Reflectance Spectra of Nanopowders of $\text{Ni}_{1-x}\text{Zn}_x\text{Fe}_2\text{O}_4$ Ferrites, *AJP Fizika XXIV*, p .26, 2018
 - [7] *N.N.Scholtz, K.A.Piskarev.* Ferrimagnetic materials for radio-frequencies, Publishing House Energy, Moscow, 2013.
 - [8] *S.Aliyeva, S.Babayev, T.Mehdiyev.* Raman spectra of $\text{Ni}_{1-x}\text{Zn}_x\text{Fe}_2\text{O}_4$ nanopowders, *JRS*; 49 (2), 271, 2018.
 - [9] *Y.V.Kasyuk, L.A.Bliznyuk, N.A.Basov, A.K.Fedotov, A.S.Fedotov, I.A.Svito.* Structure and electrophysical properties of doped zinc oxide ceramics, *International Scientific Conference*, November 22-25, Minsk, Vol. 2, pp.84-86, 2016.
 - [10] *Michael Hoppe, Sven Doring, Mihaela Gorgoi, Stefan Cramm and Martina Muller.* Enhanced ferrimagnetism in auxetic NiFe_2O_4 in the crossover to the ultrathin film limit, *Phys. Rev. B* 91, 054418 – Published 24 February 2015.
 - [11] *J. B. Goodenough.* Magnetism and the chemical bond. (Interscience Publishers, New York, 1963.
 - [12] *J. Kanamori.* “Superexchange interaction and symmetry properties of electron orbitals”, *Journal of Physics and Chemistry of Solids* 10, 87, doi: 10.1016 /0022 -3697(59) 90061-7, 1959.
 - [13] *P.W. Anderson.* “Chapter 2 - Exchange in Insulators”, in G. T. Rado and H. Suhl, *Magnetism*. Academic Press. pp. 25–83, isbn: 978-0-12-575301-2, 1963.
 - [14] *F. Shahbaz Tehrani, V. Daadmehr, A.T. Rezakhani, R. Hosseini Akbarnejad, S. Gholipour.* Structural, magnetic, and optical properties of zinc- and copper- substituted nickel ferrite nano-crystals, *Journal of Superconductivity and Novel Magnetism*, October 2012, Vol. 25, Iss. 7, pp. 2443–2455.
 - [15] *I.F.Yusibova, Sh.N.Aliyeva, T.R.Mehdiyev.* Verwey transition in Raman scattering spectra of (Ni-Zn) ferrite nanofilms, *AJP Fizika*, Vol. XXIV, №3, Section: Az, 2018, 95-100.

Received: 20.05.2019

SIMULATION SPATIAL STRUCTURE OF AMYLOID BETA-PEPTIDE (31-35)
DETERMINED BY MOLECULAR MECHANIC METHODG.A. Agaeva¹, G. Z. Najafova², N.M. Godjaev³¹*Institute for Physical Problems, Baku State University,
23, Z.Khalilov str., Baku, Azerbaijan AZ-1148*²*UFAZ under Azerbaijan State Oil and Industry University,
183, Nizami str., Baku, Azerbaijan*³*Baku State University, 23, Z.Khalilov str., Baku, Azerbaijan, AZ-1148
gulshen@mail.ru, gulyaz.najafova@ufaz.az*

The spatial structure and conformational flexibility of Amyloid β -peptide (31-35) have been investigated by molecular mechanic method. It is revealed that this molecule can exist in several stable conformational states. The energy and geometrical parameters for each of low-energy conformations are obtained. The conformationally rigid and labile segments of this molecule were revealed.

Keywords: Amyloid β - peptide (31-35), Alzheimer's disease, spatial structure, function, conformation, pentapeptide

PACS: 36.20.Ey; 87.15.Aa; 87.15.He

1. INTRODUCTION

The amyloid β - peptide (A β P) is known to cause the activation of apoptotic cascades, leading to neuronal death in Alzheimer's disease (AD) [1-4]. Amyloid β - peptide (A β P), a major protein component of the plaques, is a 39–43 amino acid peptide derived from a larger transmembrane protein, amyloid precursor protein (APP). It is well established that A β P possesses neurotoxic activity. A β P neurotoxicity has been associated to peptide self-aggregation, which leads to the formation of amyloid-like fibrils and eventually to neuronal cell death through apoptosis. Some recent studies confirmed that A β (31–35), i.e. IIGLM, (Ile–Ile–Gly–Leu–Met), which is a shorter sequence of A β P, can also induce apoptosis in the cortical and hippocampal neurons as A β (25–35) does has also been demonstrated in neuronal PC 12 cells and rat cerebellar granule cells [1-4]. In work [2] are used X- ray diffraction and electron microscopy to investigate the structure of the assemblies formed by A β (25-35) peptides and of various length sequences. In this article it is proposed that the tachykinin- like A β (31-35) peptide is a turn exposed at the A β oligomer surface where it could interact with the ligand- binding site of the tachykinin G- protein-coupled receptor [2].

A synthetic fragment (31–35) of β - amyloid peptide was used in cultured cortical neurons to examine whether this smaller sequence could trigger apoptotic degeneration *in vitro* by using morphological, biochemical and flow- cytometric examinations. On the other hand, it is known that this Ab derived pentapeptide although not exhibiting aggregation phenomena, is able to determine a large number of toxic effects, including the activation of apoptotic pathways in cultured cortical neurons [4]. Here, in order to gain more insight into the mechanism of spatial formation of A β (31-35) peptide in nonpolar solution, which particularly stabilizes α -helical conformation, we studied the secondary-structural elements of the A β (31-35) peptide in vacuum and

polar solution by molecular mechanics simulations. The α -helical environment around Met35 was completely abolished as indicated by circular dichroism (CD) -spectroscopy [5]. The study of the conformational properties of A β peptides in their soluble form constitutes a basic approach to design of molecules with "anti-amyloid" activity and to develop anti- Alzheimer therapies. The diversity of biological functions of peptide molecule is undoubtedly connected to its conformational properties. The determination of conformational particularities of biologically active peptide molecules is a necessary stage in the study structured-functional relationships of these molecules. It is difficult to predict the active peptide conformation, which realized in complex with the receptor, since most of small linear molecules exist in aqueous and other environments as set of low-energy conformations with comparative stability. In order to elucidate the mechanism of action of the peptide the investigation of the native three dimensional structure is necessary that first of all requires the information about of the full set of low energy and consequently the potentially and physiologically active conformations of this molecule. The major aim of the present article is the investigation of the three-dimensional structure and conformational flexibility for A β (31-35), with the purpose of getting insight into basic structural requirement that determine ligand-receptor interaction. The conformational properties of A β (31-35) peptide molecule have been investigated by molecular mechanic method, which allow to determine a whole set of energetically preferred conformers of peptide molecule.

2. METHOD

Molecular mechanics (MM) study of A β (31-35) conformation involves multistaged extensive computations of even-increasing fragments, with a set stable forms of each preceding step used as a starting set in the next step. Only those conformations are

retained whose energies are smaller than some cut-off values. The sequential method was used, combining all low-energy conformations of constitutive residues [5]. The conformational potential energy of a molecule is given as the sum of the independent contributions of nonbonded, electrostatic, torsional interactions and hydrogen bonds energies. The first term was described by the Lennard-Jones 6-12 potential with the parameters proposed by Scott and Scheraga. The electrostatic energy was calculated in a monopole approximation corresponding to Coulomb's law with partial charges of atoms as suggested by Scott and Scheraga. An effective dielectric constant value $\epsilon=1$ for vacuum, $\epsilon=4$ for membrane environment and $\epsilon=80$ for water surrounding is typically used for calculations with peptides and proteins, which create the effects of various solutions on the conformations of peptides by MM method [5]. The hydrogen bond energy is calculated based on Morse potential Bonding lengths and angles are those given by Corey and Pauling [6] and are kept invariable; the ω angle of the peptide bond was fixed at 180° . The torsional energy was calculated using the value of internal rotation barriers given by Momany et al [7]. Computations were carried out on the computer using universal programs complex [8]. The dihedral rotation angles were counted according to the IUPAC-IUB [9]. Symbols are used to represent the regions of conformational space situated around backbone dihedral angles values (ϕ , ψ) are: R (ϕ , $\psi=-180^\circ-0^\circ$), B ($\phi=-180^\circ-0^\circ$, $\psi=0^\circ-180^\circ$), L (ϕ , $\psi=0^\circ-180^\circ$) and P ($\phi=0^\circ-180^\circ$, $\psi=-180^\circ-0^\circ$). Rotamer 1, 2, 3: side chain bonds $\chi_1=60^\circ$, 180° , -60° respectively. Each conformational state of a residue is characterized by $X_{i,j}^n$..., where X characterizes the backbone ϕ , ψ angle regions (B, R, L or I), n is the number of a residue in the sequence and subscripts i, j, ... specify the position of the side chain χ_1 , χ_2 ..., respectively, so that i or j = 1 corresponds to the angle χ (χ_1 or χ_2) in the range 0° to 120° ; a value of two corresponds to the angle 120° to -120° and three to -120° to 0° .

3. RESULTS AND DISCUSSION

Conformational study of the pentapeptide A β (31-35) was carried out in three stages, in each of which were used results of preceding stage. In turn, stages are divided on consecutively decided structured problems. The first stage of calculation included consideration of conformational possibilities of dipeptide fragments Ile-Ile and Leu-Met according to the calculation scheme. Calculations of fragments were conducted for the reason reducing a number of possible initial variants for pentapeptide. But the initial variants of the small fragments were formed on the base of low-energy conformations of the corresponding mono-peptides. The optimal backbone forms in the relative 0-5 kcal/mole energy interval of the pentapeptide Ile-Ile-Gly-Leu-Met-NH₂ are presented in Table 1. Then on the base low-energy conformations of the fragments were calculated the stable conformations of the pentapeptide with the C-

terminal amide group NH₂. The variants for pentapeptide were taken into account conformational particularities of both dipeptides and Gly mono-peptide. Besides, in initial variants of the pentapeptide were taken different orientations of the side chains in peptide chain depending on the type of 20 backbone forms. Only α -helical conformations of these forms with different intermolecular interactions are entered in the interval of relative energy 0-3 kcal/mole. Other low-energy conformations belong to the 11 backbone forms (table1).

The energy contributions of all calculated types of interactions of preferred conformations of the pentapeptide Ile-Ile-Gly-Leu-Met-NH₂ are shown in table2 [11].

In the α -helical global conformation carbonyl group of backbone of Ile1 is very approach with NH group of Met 5 that favours a forming the efficient interactions between them, which promotes shaping the hydrogen bond. It is necessary to note that the essential energy contributions of specific interactions between residues Ile1 and Leu4 are stabilize factor of the conformational stability of these conformations. The molecular model of the preferred conformation of pentapeptide A β (31-35) is represented in the fig. 1.

The spatial model of pentapeptide were built in HyperChem 8.01 [10]. The electrostatic interactions are eliminated between N- and C-terminal groups that is reflected on the value of energy contribution of the interresidue interactions of the residues. As a result of the calculation for this pentapeptide most favored turns out to be only one conformation with completely turned form of chains. In this conformation C-terminal pentapeptide does not prevent a formation stable intermolecular hydrogen relationship between side chains of the terminal residues. The energy of intra- and interresidues interactions of three stable conformations of the Ile-Ile-Gly-Leu-MetNH₂ pentapeptide is presented in Table 3.

Other optimal conformations are not important for the collecting with the receptor. The values of dihedral angles of the lowest energy conformations of the A β (31-35) pentapeptide are presented in table 4.

Then possible expect that the most probable biologically active conformation for A β (31-35) pentapeptide is conformation with the form of the frame RRRRR, stabilized by intramolecular hydrogen bond between backbone atoms of Ile1 and Met5.

Thus, the conformational study of A β (31-35) pentapeptide enabled the estimation of the role of each of the substituted residues in the structure formation have been carried out. The comparison of specific features of low-energy conformations of pentapeptide revealed general structural criteria of this molecule, which may be necessary for their biological activity.

To summarize, the results of the theoretical conformational analysis of A β (31-35) combined with the data on their biological activity indirectly supported by physicochemical data allow an assumption that, when binding to receptor, this pentapeptide prefer the conformation with α alpha-helical structure.

Table 1.

The optimal backbone forms in the relative energy interval of the pentapeptide Ile-Ile-Gly-Leu-Met-NH₂.

№	Backbone form	The relative energy interval (kcal/mole)					
		0-1	1-2	2-3	3-4	4-5	>5
1.	BBBBB	-	-	-	-	2	79
2.	BBRBB	-	-	-	-	2	79
3.	BBRRR	-	-	-	-	3	78
4.	BBRBR	-	-	-	-	5	76
5.	BRBBB	-	-	-	2	8	71
6.	BRRBB	-	-	-	-	1	80
7.	BRBRR	-	-	-	2	2	77
8.	BRRRR	-	-	-	-	1	80
9.	RBBBB	-	-	-	1	2	78
10.	RBRRR	-	-	-	-	1	80
11.	RBBRR	-	-	-	2	2	77
12.	RBBBR	-	-	-	1	2	78
13.	RRBBB	-	-	-	-	2	79
14.	RRRBB	-	-	-	2	2	77
15.	RRBRR	-	-	-	2	1	77
16.	RRRRR	7	2	2	-	1	71
17.	BBPBR	-	-	-	1	-	79
18.	RBLBB	-	-	-	1	1	78
19.	RRPRR	-	-	-	1	-	79
20.	RBPBR	-	-	-	1	2	77

Table 2.

Energy contributions of all calculated types of interactions of preferred conformations of the pentapeptide Ile-Ile-Gly-Leu-Met-NH₂.

№	Conformation	Energy contributions (kcal/mole)				E _{rel}
		E _{nb}	E _{el}	E _{tor.}	E _{abs.}	
1.	R ₃₂ R ₃₂ RR ₂₂ R ₃₂	-22.1	4.1	3.0	-15.0	0
2.	R ₃₂ R ₃₂ BR ₃₂ R ₃₂	-18.2	4.3	1.8	-12.0	3.0
3.	R ₃₂ B ₂₂ BR ₃₂ R ₃₂	-18.0	4.3	1.8	-11.9	3.1
4.	B ₂₂ R ₃₂ BB ₂₂ B ₃₂	-19.2	4.0	3.4	-11.9	3.1
5.	B ₁₂ B ₁₂ PB ₂₂ R ₃₂	-19.0	3.8	3.4	-11.8	3.2
6.	R ₂₂ B ₁₂ LB ₃₂ B ₃₂	-19.3	4.2	3.4	-11.7	3.3
7.	B ₂₂ R ₃₂ BR ₃₂ R ₃₂	-18.5	4.2	2.9	-11.4	3.6
8.	R ₃₂ B ₂₂ BB ₃₂ B ₃₂	-17.0	4.0	1.8	-11.3	3.7
9.	R ₂₂ R ₂₂ PR ₃₂ R ₃₂	-17.2	4.4	1.6	-11.2	3.8
10.	R ₂₂ B ₁₂ BR ₃₂ R ₂₂	-17.1	4.3	1.8	-11.1	3.9
11.	B ₁₂ R ₂₂ BR ₂₂ R ₂₂	-17.2	4.2	2.1	-11.0	4.0
12.	R ₂₂ B ₁₂ PB ₂₂ R ₃₂	-17.6	3.8	2.7	-11.0	4.0
13.	R ₃₂ R ₃₂ BB ₃₂ B ₃₂	-16.5	4.2	2.0	-10.3	4.6
14.	B ₂₂ B ₂₂ BB ₃₂ B ₃₂	-16.2	3.8	2.0	-10.4	4.6

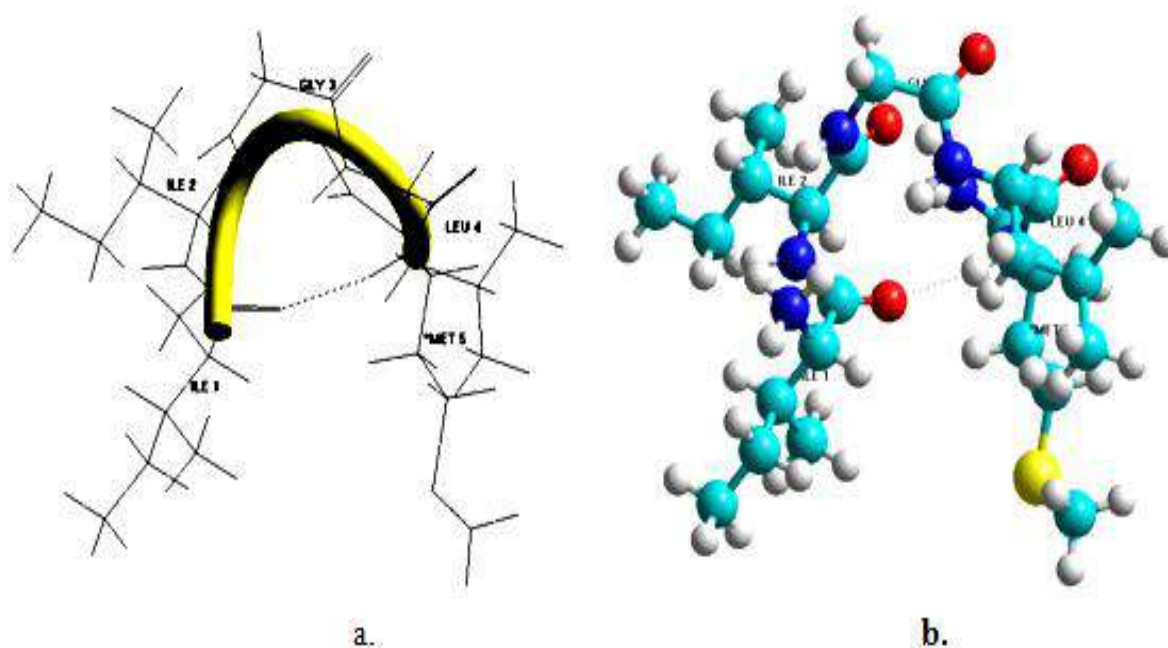


Fig. 1. The molecular model of lowest conformation of Ile-Ile-Gly-Leu-MetNH₂ A β (31-35) pentapeptide: a) secondary structure – α -helix turn shown in yellow thick line, b) in balls and cylinders. Hydrogen bond is shown dashed line.

Table 3.

The energy of intra- and interresidues interactions of the stable conformations of the Ile-Ile-Gly-Leu-MetNH₂ pentapeptide. 1- R₂₂R₃₂RR₂₂R₃₂; 2- B₂₂R₃₂BB₃₂B₂₂; 3- B₂₂R₃₂BB₃₂B₂₂

	Ile ¹	Ile ²	Gly ³	Leu ⁴	Met ⁵	
1	0.8	-2.8	-2.0	-3.7	-2.8	
2	-0.3	-2.7	-2.2	-2.8	-0.1	
3	-0.2	-2.5	-1.3	-3.0	0.0	
		1.6 0.3 0.3	0.7 -0.8 -0.7	-1.1 -1.3 -1.7	-2.5 0.0 -0.1	Ile ²
			1.2 1.2 1.2	0.7 -0.5 -1.2	-0.7 -0.9 -0.5	Gly ³
				-1.0 -0.7 -0.7	-3.7 -2.2 -1.6	Leu ⁴
					-2.1 -2.5 -2.4	Phe ⁵

Table 4.

The values of dihedral angles of the lowest energy conformations of the A β (31-35) pentapeptide.

Aminoacid	Dihedral angle	Lowest-energy conformations		
		R ₂₂ R ₃₂ RR ₂₂ R ₃₂	B ₂₂ R ₃₂ BB ₃₂ B ₂₂	B ₂₂ R ₃₂ BR ₃₂ R ₃₂
Ile	φ	-71	-148	-146
	ψ	-52	147	139
	ω	177	179	179
	χ_1	-61	185	178
	χ_2	184	186	185
	χ_3	177	169	168
	χ_4	184	187	186
Ile	φ	-70	-92	-106
	ψ	-34	-59	-58
	ω	-181	179	184
	χ_1	-61	-59	-58
	χ_2	183	186	187
	χ_3	177	173	174
	χ_4	184	189	189
Gly	φ	-59	-80	-82
	ψ	-39	91	95
	ω	-177	177	189
Leu	φ	-81	-108	-98
	ψ	-63	107	-60
	ω	-173	182	174
	χ_1	175	197	-56
	χ_2	64	172	176
	χ_3	60	191	186
	χ_4	58	180	180
Nle	φ	-92	-121	-120
	ψ	-52	141	-60
	ω	-181	181	181
	χ_1	-60	-60	-61
	χ_2	180	181	180
	χ_3	180	181	180
	χ_4	181	180	180
E _{total} (kcal/mole)		-15.7	-11.87	-11.39

4. CONCLUSION

Thus, on the basis of conformational studies of amyloid β -peptide (31-35) molecule it has been suggested that the biologically active conformation of this peptide at its receptor is turned structure in solution. The obtained data allow one conclude that, in

structures, where is formed a beta-turn at the *N*-terminal segment and residues have only one local minimum. The investigation results therefore indicate that a concrete type of the β -peptide (31-35) structure will essentially depend on the conditions under which the given molecule functions.

- [1] F.Misiti, M.E.Clementi, G.Tringali, M.Vairano, Federica Orsini, Michela Pezzotti, Pierluigi Navarra, Bruno Giardina, Giacomo Pozzoli. *Neurochemistry International* 49, p. 525, 2006.
- [2] J.P.Bond, Sean P.Deverin, Hideyo Inouye, Omar M.A. El-Agnaf, Martha M.Teeter and

- Daniel A.Kirschner. *Journal of Structural Biology* 141, 156, 2003.
- [3] F.Misiti, Beatrice Sampaiolese, Michela Pezzotti, Stefano Marini, Massimo Coletta, Lia Ceccarelli, Bruno Giardina, M.E. Clementi. *Neurochemistry International* 46, p. 575, 2005.

- [4] *M.E. Clementi, Stefano Marini, Massimo Coletta, Federica Orsini, Bruno Giardina, F.Misiti.* "FEBS Letters 579, 2913, 2005.
- [5] *J.Kanski, M.Aksenova, C.Schoneich, D.A.Butterfield.* Free Radical Biology and Medicine, 32(11), 1205, 2002.
- [6] *R.A. Scott, H.A. Scheraga.* J.Chem.Phys.,45, 2091, 1966.
- [7] *F.A. Momany, R.McGuire, A.W. Burgess, H.A. Scherag.* J.Phys.Chem., 79, 2361, 1975.
- [8] *I.S. Maksumov, L.I. Ismailova, N.M. Godjaev.* J.Struct. Khim. (in Russian), 1983, vol. 24, p.p. 147-148, 1983.
- [9] IUPAC-IUB Quantity. Units and Symbols in Physical Chemistry 39, Blackwell Scientific Publications, Oxford, 1988.
- [10] Chem 3D Pro. "Molecular Modeling and Analysis," Cambridge Soft Corporation, 875 Massachusetts, 02139, USA, 2005.
- [11] *G.A. Agaeva, G.Z. Najafova.* "Conformational analysis of β -amiloid peptid (31-35) molecule". I International Scientific Conference of Young Researchers. Azerbaijan. May, p. 34-35, 2017.

Received: 10.06.2019

SYNTHESIS AND CHARACTERIZATION OF THE $\text{BiTe}_{1-x}\text{Se}_x\text{I}$ SOLID SOLUTIONS SERIESZIYA S. ALIEV^{1,2}¹*G.M. Abdullayev Institute of Physics of Azerbaijan NAS
131, H. Javid ave., AZ1143 Baku, Azerbaijan*²*Azerbaijan State Oil and Industry University, 20, Azadlig ave., AZ1010 Baku, Azerbaijan
ziyasaliev@gmail.com; ziya.aliev@asoiu.edu.az*

Nowadays, the bismuth tellurohalides and their derivatives are one of most studied and required materials in the condensed matter physics community thanks to giant-spin orbit Rashba-type spin-splitting in their free-electron-like surface states. This work describes the synthesis and characterization of the $\text{BiTe}_{1-x}\text{Se}_x\text{I}$ solid solutions series based on the BiTeI , which is known as a giant- Rashba semiconductor. The existence of the $\text{BiTe}_{1-x}\text{Se}_x\text{I}$ solid solutions series (γ_1 and γ_2) experimentally confirmed by powder X-ray diffraction (PXRD) and scanning electron microscope equipped with energy dispersive X-ray spectrometer (SEM-EDS). Phase diagram of the system were plotted based on experimental data from Differential Thermal Analysis (DTA).

Keywords: phase diagram; materials synthesis; bismuth seleniodide; bismuth telluroiodide; solid solutions

PACS: 81.20.-n, 81.30.Bx

1. INTRODUCTION

Since the existence of giant three-dimensional (3D) bulk Rashba-type spin splitting has recently been reported in the polar layered non-centrosymmetric BiTeI [1-2], the bismuth containing tellurohalides became one of the much more attractive materials in condensed matter physics [3-6]. These materials have been reported to have a strong spin-orbit interaction effect that reveals new paths for the realization of spin-based electronic devices based on them. On the other hand, sulfo- and selenohalides of a group 15 metals have been intensively studied over the last four decades due to their intriguing ferroelectric, piezoelectric and semiconducting properties [7-11]. The growing interest to these materials steams from their intriguing electronic properties which make them perspective source materials for spin-based electronics and ferroelectric, thermoelectric, photovoltaic, etc., devices [1, 2, 9-11].

The rational design and elaboration of such ternary or quaternary new phases, in particular, solid solutions having a non-centrosymmetric crystal structure and variable chemical compositions by cation and anion substitutions is of significant interest from the point of view optimized properties. Considering increasing interest to this class of materials, the thorough investigation of phase diagrams for the respective element systems is of particular importance to find proper starting composition for the elaboration of materials with optimized properties [13-14].

Here, we present the experimental study of the phase BiTeI - BiSeI system. This study can shed light on the chemical design of the new phases with variable compositions based on the starting multifunctional compounds of the systems namely, BiTeI and BiSeI .

The ternary compound BiTeI was found in the $\text{Bi}_2\text{Te}_3\text{-BiI}_3$ system. This system includes only this

compound melts congruently at 828 K and crystallizes in a hexagonal system with space group $P3m1$ and lattice parameters $a = 4.3392(1)$, $c = 6.854(1)$ Å and $z = 1$ [15]. Another starting compound, BiSeI was reported along the quasi-binary $\text{Bi}_2\text{Se}_3\text{-BiI}_3$ system that has been investigated by different authors so far. The literature data on this binary system until 2004 were reviewed by Oppermann [16]. This compound melts incongruently at 818 K and crystallizes in the SbSI -type orthorhombic crystal system with space group $Pnma$ and lattice $a = 8.697(2)$, $b = 4.221(1)$, $c = 10.574(2)$ Å and $z = 4$ [17].

2. EXPERIMENTAL PART

2.1. Synthesis

Starting BiSeI and BiTeI were synthesized from the elements of a high purity grade (not less than 99.999%) in sealed ($\sim 10^{-3}$ Pa) silica ampoules at 850 K. Synthesis processes of the compounds performed in a split tube furnace by a specially designed method that takes into account of the high volatility of iodine. The syntheses were performed in an inclined three-zone furnace, with two hot zones kept at 850 K, whereas the temperature of the cold zone was 400 K. After the bulk of the iodine reacted, the ampoules were relocated such that the products melted at 850 K. The melts were stirred at these temperatures by slightly shaken of ampoules and then cooled in the furnace. Because of BiSeI melt by peritectic reactions, it was further annealed at 770 K for 250 h in order to complete homogenization. All the considered samples along the BiSeI - BiTeI (total mass = 0.5g) were prepared from preliminary synthesized ternary compounds. After melting, the alloys were annealed at 730 K for two weeks.

2.2. Analysis

DTA, PXRD, and SEM-EDS techniques were employed to test the purity of the synthesized starting compounds and analyze the alloys. Thermal analysis was carried out using a NETZSCH 404 F1 Pegasus system from room temperature up to 1000 K with a heating rate of 10 K min^{-1} . Temperatures of thermal effects were taken from the heating thermograms. The PXRD patterns were recorded on a Bruker D8 ADVANCE diffractometer with $\text{Cu-K}\alpha_1$ radiation within the range of $2\theta = 5^\circ \div 75^\circ$. The microstructures and equilibrium compositions for the some selected samples were determined by Tescan Vega 3 SBH scanning electron microscope equipped with ThermoScientific UltraDry Compact EDS Detector.

3. RESULTS AND DISCUSSIONS

The phase diagram of BiSeI-BiTeI system was plotted based on the DTA, PXRD and SEM data of the equilibrated alloys (fig. 1). The system was found to be non-quasi-binary. Apparently, this section is represented by the liquidus surface of the β -phase in the wide range of composition (0-75 mol% BiTeI). The β -phase appears here due to this section is a quasi-binary part of the $\text{Bi}_2\text{Te}_3\text{-BiSe}_3\text{-BiI}_3$ system. The β -phase is a continuous solid-solution area of the $\text{Bi}_2\text{Se}_3\text{-Bi}_2\text{Te}_3$ system and can be shown as $\text{Bi}_2\text{Se}_{3-x}\text{Te}_x$ ($0 \leq x \leq 1$) [18]. The detailed investigation of the phase relationships of the different phases, including that β -phase along the $\text{Bi}_2\text{Te}_3\text{-BiSe}_3\text{-BiI}_3$ system is under investigation and will be published soon. In the subsolidus region, two wide solid-solution areas were revealed based on BiSeI (γ_1) and BiTeI (γ_2). The primary crystallization of the γ_2 -phase based on the

BiTeI occurs in the BiTeI-rich part of the system. A horizontal line at 760 K reflects the invariant transition reaction (U) $L + \beta \leftrightarrow \gamma_1 + \gamma_2$ that leads to the formation of biphasic $\gamma_2 + \gamma_1$ area in the subsolidus region. The expansion of this biphasic area was measured to be 30-45 mol% BiTeI at 760 K. The existence of these mono- and biphasic areas along this section were confirmed by PXRD and SEM micrographs (figs. 2 and 3 a-c). Fig. 2 displays the PXRD patterns of the selected alloys along the BiSeI-BiTeI section. Evidently, the PXRD patterns of alloys #1 and #2 are qualitatively similar to BiSeI, whereas the patterns of samples #5, #6 and #7 are entirely composed by diffraction peaks of BiTeI. On the other hand, it was observed that upon increasing the BiTeI content in both the γ_1 - and γ_2 -phases, there is negligible shifting in the peak positions on respective XRD patterns (alloys #1, #2 and #5, #6, #7) towards smaller angles. This fact is typical for the systems containing wide solid-solutions areas, and further confirms the existence and homogeneity areas of the γ_1 - and γ_2 -phases. The PXRD patterns for the alloys #3 and #4 display their biphasic content with clearly observed diffraction peaks typical for both starting BiTeI and BiSeI (distinguished by black triangles and blue circles in fig. 2, respectively). The phase constitutions of the BiSeI- BiTeI alloys are further confirmed in SEM micrographs of the alloys #2, #4 and #5 (figs. 3 a-c). Obviously, mono- and biphasic microstructures were observed in the SEM images for the alloys #2, #5 and #4, respectively. The microstructure of the alloy #4 (fig. 3 b) displays clearly co-crystallized γ_1 - and γ_2 - phases whereas, alloys #2 and #5 (Figs. 3 a, c) were found to be single phase according to pure γ_1 - and γ_2 - phases, respectively.

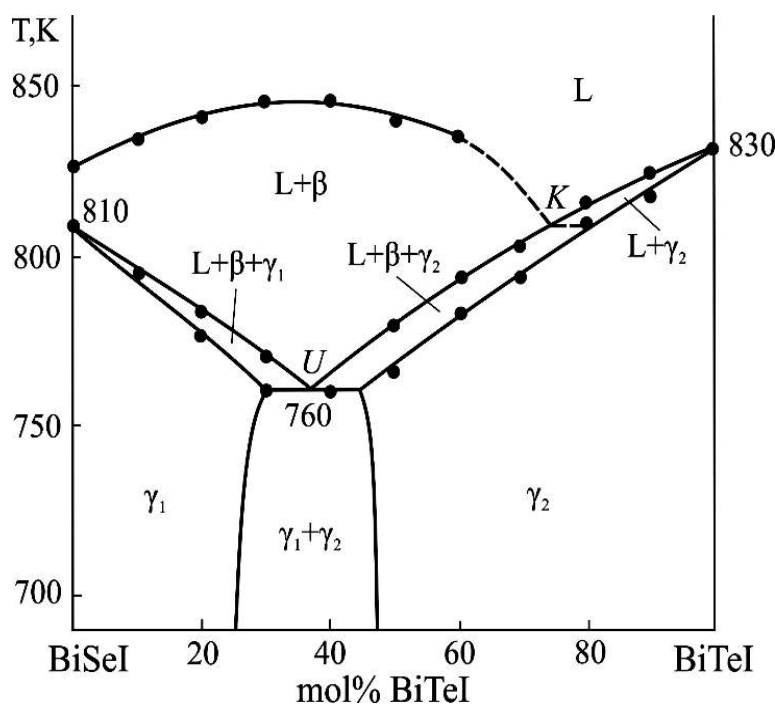


Fig. 1. The phase diagram of the BiSeI – BiTeI system

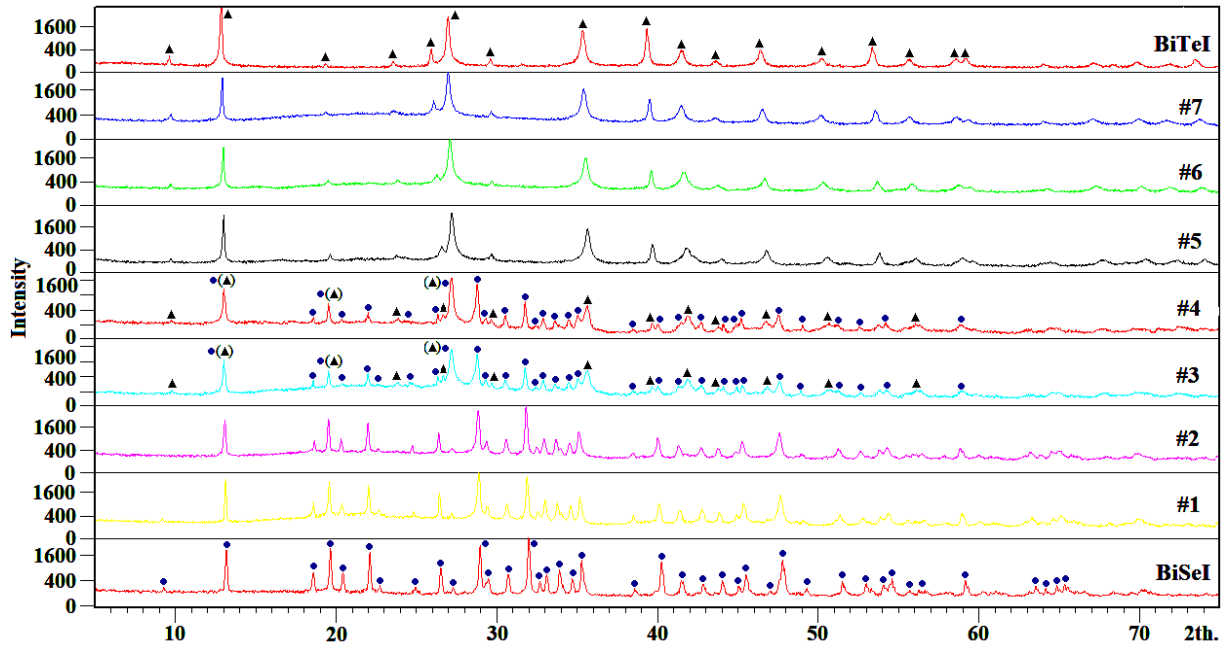


Fig. 2. PXRD patterns for different alloys in the BiSeI- BiTeI section: #1, 10 mol % BiTeI; #2, 20 mol %; #3, 30 mol %; #4, 40 mol %; #5, 50 mol %; #6, 60 mol %; #7, 80 mol

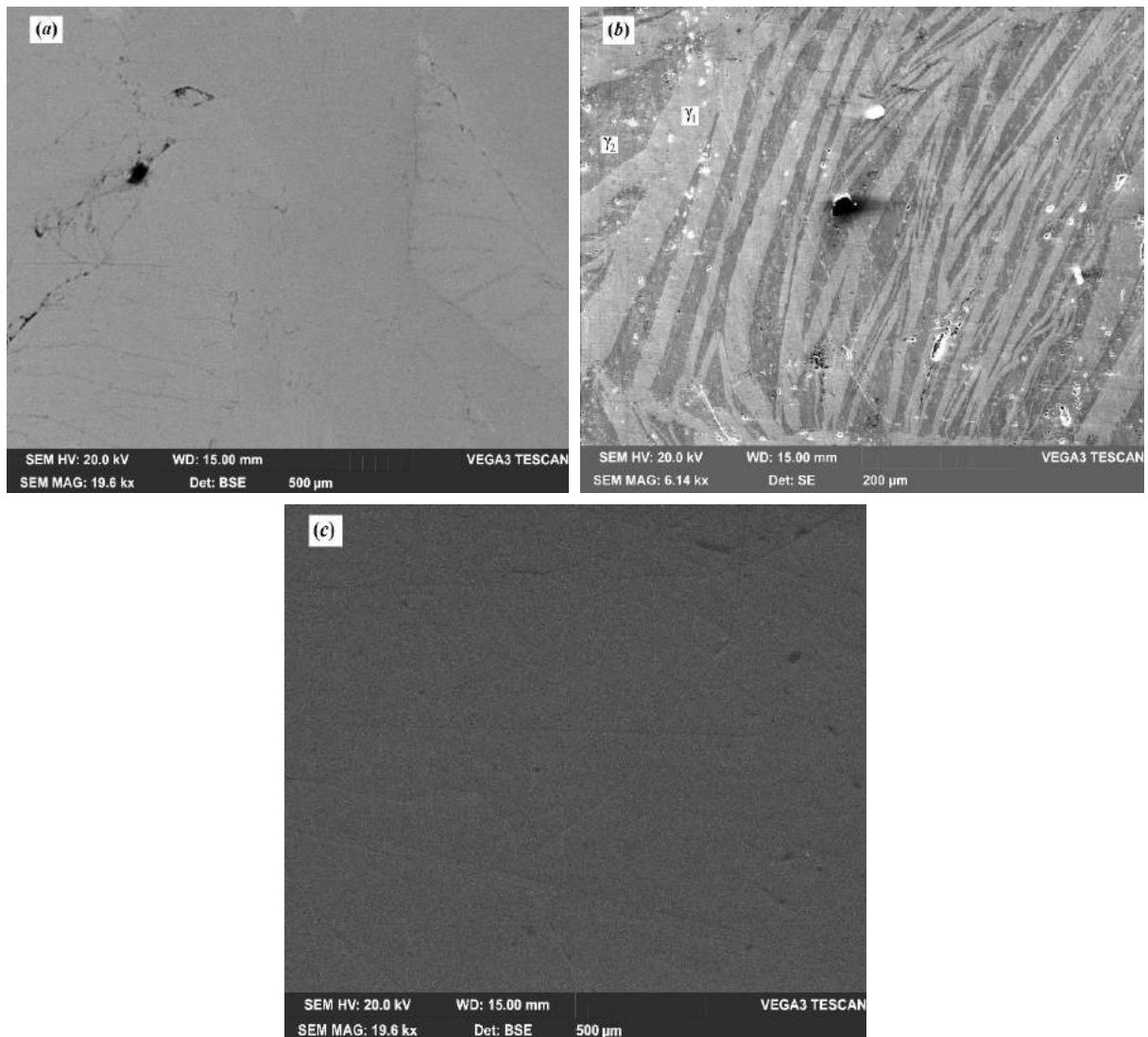


Fig. 3. SEM micrographs of the selected alloys #2 (a); #4 (b) and #5 (c) in the BiSeI- BiTeI section

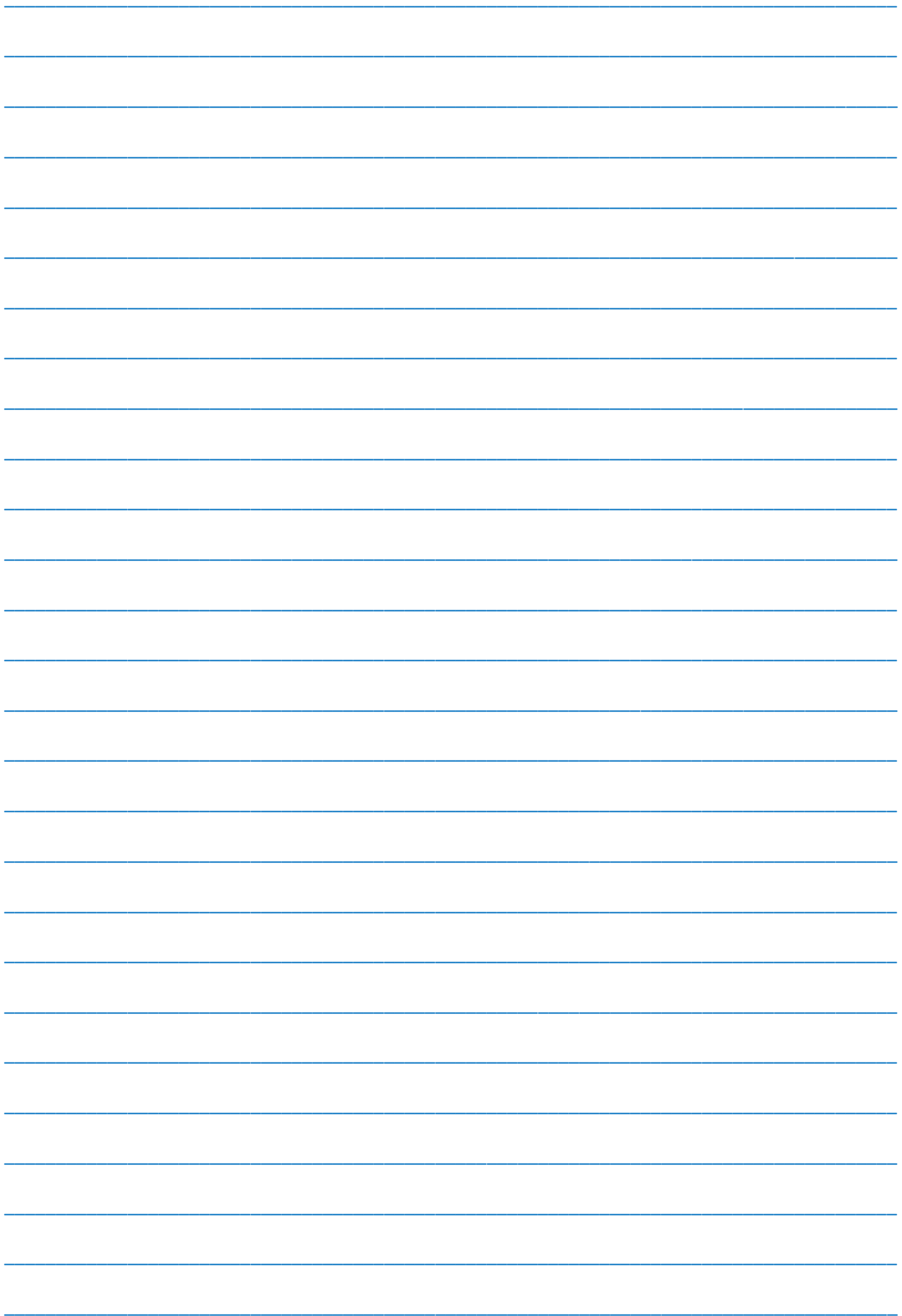
4. CONCLUSION

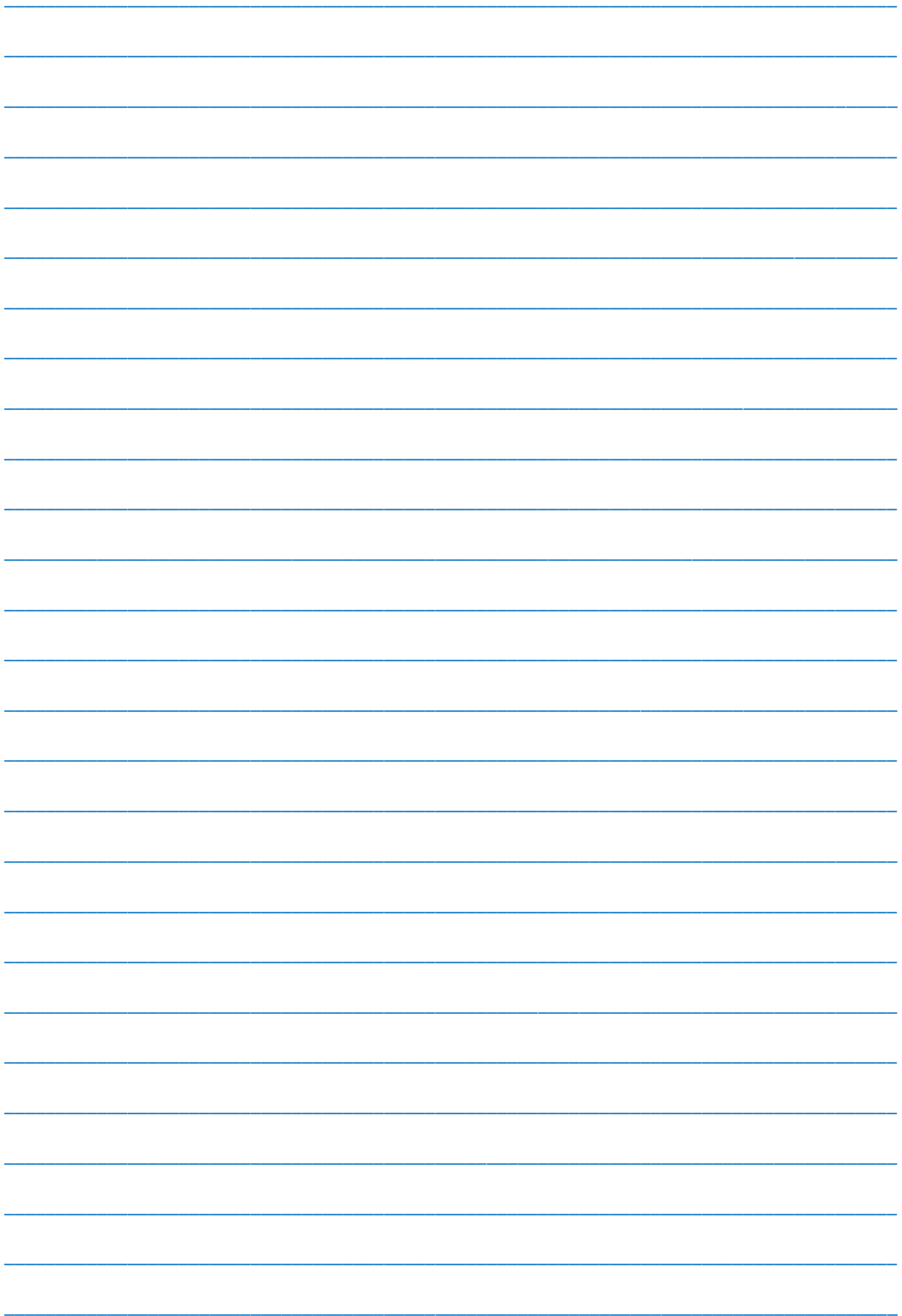
The phase equilibrium in the BiSeI- BiTeI system was studied experimentally, shown that it is a non-quasi-binary one and features by wide solid solution areas based on the starting BiSeI and BiTeI compounds, respectively. The obtained data collected in this work, provides very valuable information for

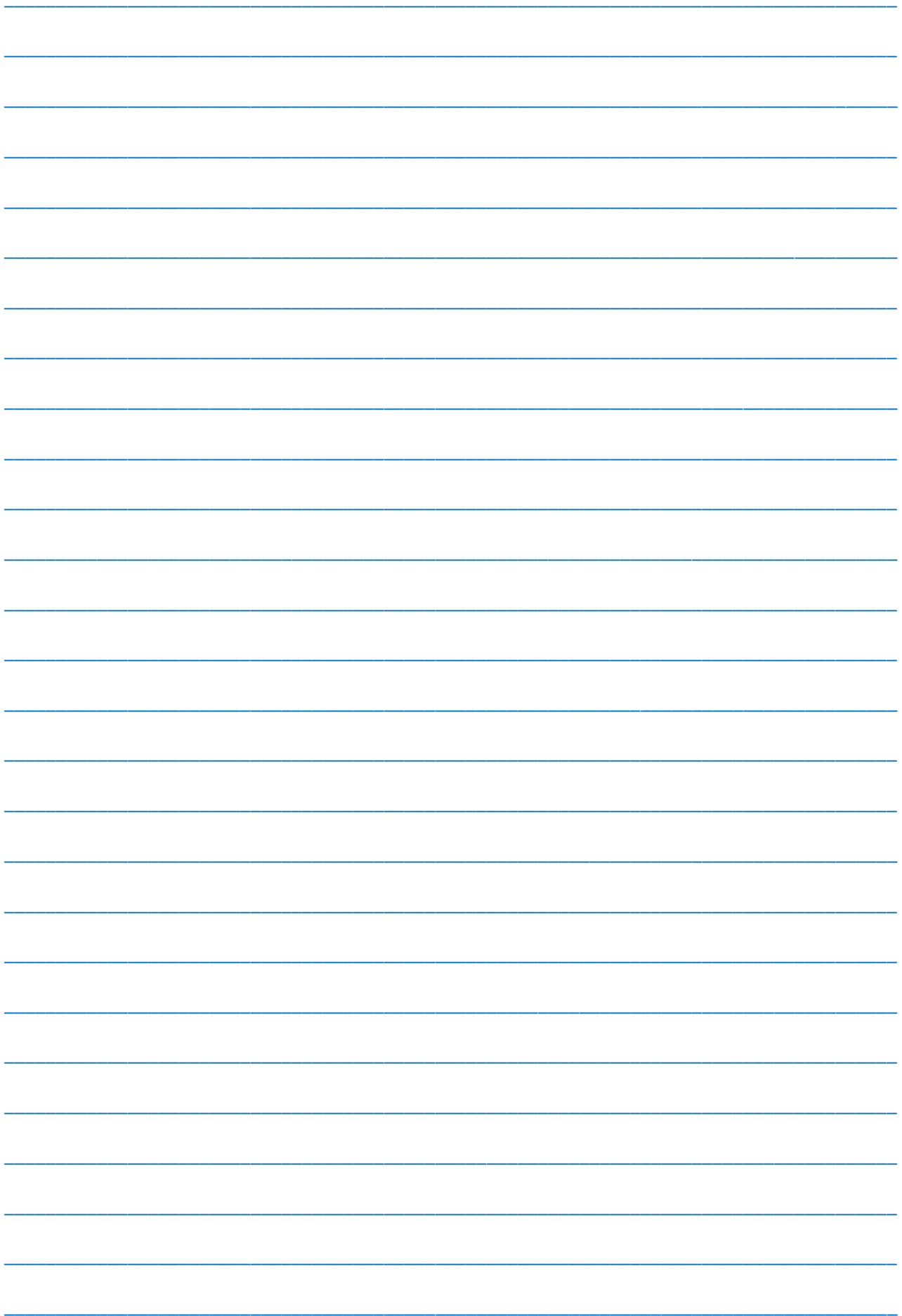
optimizing the synthesis and growth conditions of newly obtained materials. Particularly, the considered system is of significant importance in terms of the rational design of new $\text{BiTe}_{1-x}\text{Se}_x\text{I}$ solid solutions (γ_2 -phase), which are expected to exhibit Rashba type spin splitting in the electronic structure similar to undoped BiTeI, which is known as a giant- Rashba semiconductor.

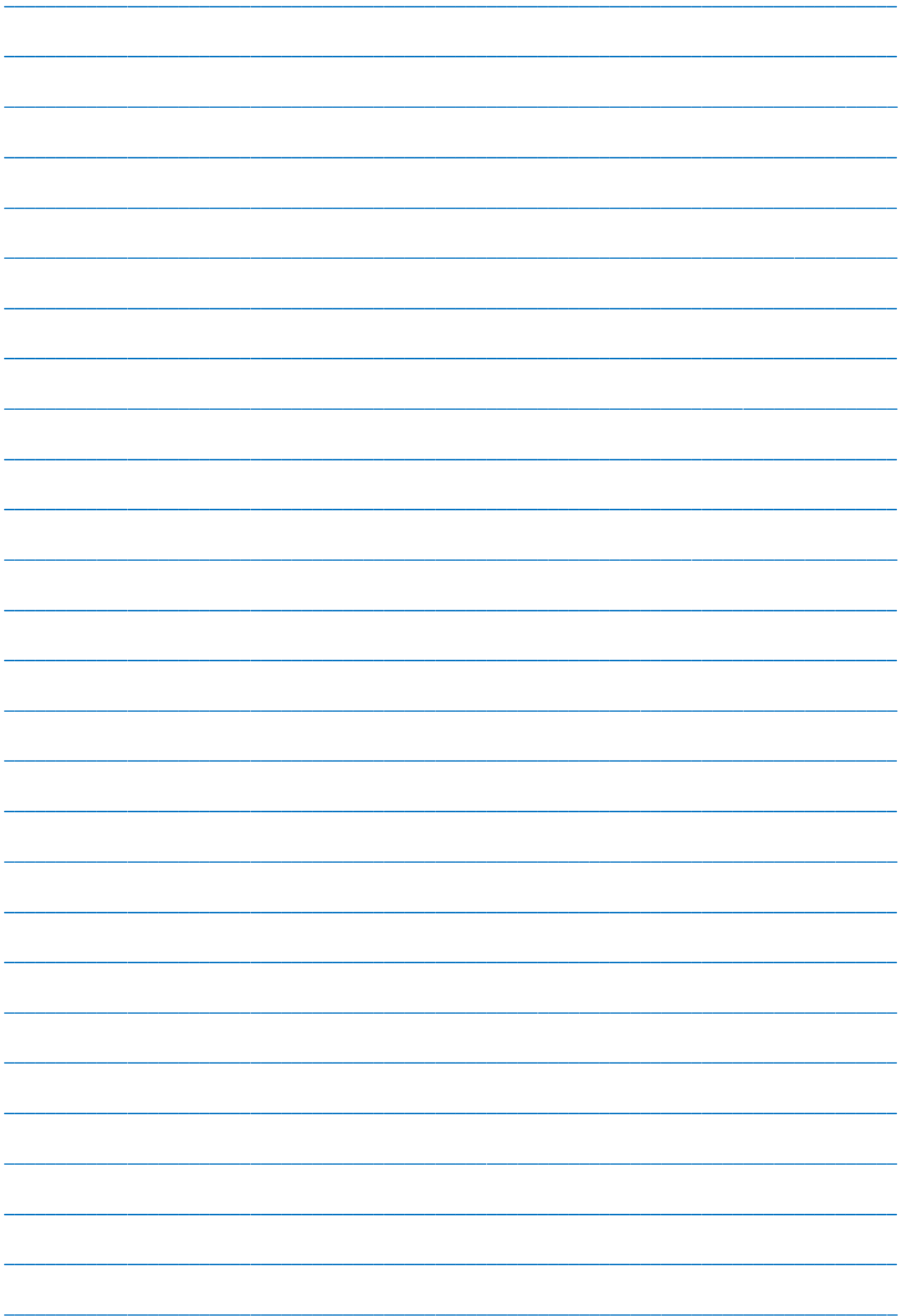
-
- [1] K.Ishizaka, M.S.Bahramy, H.Murakawa, M.Sakano, T.Shimajima, T.Sonobe, K.Koizumi, S.Shin, H.Miyahara, A.Kimura, K.Miyamoto, T.Okuda, H.Namatame, M.Taniguchi, R.Arita, N.Nagaosa, K.Kobayashi, Y.Murakami, R.Kumai, Y.Kaneko, Y.Onose, Y.Tokura. *Nat. Mater.* 10, 521, 2011.
 - [2] G.Landolt, S.V. Eremeev, Yu. M. Koroteev, B.Slonski, S.Muff, T.Neupert, M.Kobayashi, V.N. Strocov, T.Schmitt, Z.S. Aliev, M.B. Babanly, I.R. Amiraslanov, E.V. Chulkov, J. Osterwalder, J.H. Dil. *Phys. Rev. Lett.* 109, 116403 2012.
 - [3] M.S. Bahramy, B.J. Yang, R. Arita, N.Nagaosa. *Nature Commun.* 3, 679, 2012.
 - [4] G.Landolt, S.V. Eremeev, O.E. Tereshchenko, S. Muff, B. Slonski, K.A. Kokh, M. Kobayashi, T.Schmitt, V.N. Strocov, J.Osterwalder, E.V. Chulkov and J.H. Dil. *New J. Phys.* 15, 085022, 2013.
 - [5] S.Fiedler, T.Bathon, S.V.Eremeev, K.A.Kokh, O.E.Tereshchenko, E.V.Chulkov, P.Sessi, H.Bentmann, M.Bode, F.Reinert. *Phys. Rev. B* 92, 235430, 2015.
 - [6] M.S. Bahramy, N.Ogawa. *Adv. Mater.* 29, 1605911, 2017.
 - [7] A. Audzijonis, R. Sereika R. Žaltauska., *Solid State Commun.* 147, 88-89, 2008.
 - [8] K. Łukaszewicz, A. Pietraszko, M. Kucharska, *Ferroelectrics.* 375,170-177, 2008.
 - [9] A.Audzijonis, G.Gaigalas, L.Žigas, R.Sereika, R.Žaltauskas, D.Balnionis, A.Rėza. *Phys. Status Solidi B* 246, 7, 1702–1708, 2009.
 - [10] A.Audzijonis, R.Zaltauskas, R.Sereika, L.Zigas, A.Reza, J. *Phys. Chem. Solids* 71, 884–891, 2010.
 - [11] A.M.Ganose,K.T.Butler,A.Walsh, D.O.Scanlon. *J.Mater. Chem. A*, 4, 2060-2068, 2016.
 - [12] H. Zhang, C.X. Liu, X.L. Qi, X. Dai, Z. Fang, S.C. Zhang. *Nat. Phys.* 5, 438–442, 2009.
 - [13] G.Gottstein. *Physical Foundations of Materials Science.* Springer. XIV, p. 502, 2004.
 - [14] M.B. Babanly, E.V. Chulkov, Z.S. Aliev, A.V. Shevelkov, I.R. Amiraslanov. *Russ. J. Inorg. Chem.*, 62, 1703–1729, 2017.
 - [15] A.V.Shevelkov, E.V.Dikarev, R.V.Shpanchenko, B.A. Popovkin. *J. Solid State Chem.* 114, 379-384, 1995.
 - [16] H.Oppermann,U.Petasch,P.Schmidta,E.Keller, V.Kramer. *Z.Naturforsch.* 59b, 727 –746, 2004.
 - [17] T.P. Braun, F.J. DiSalvo. *Acta Crystallogr. C* 56, e1- e2, 2000.
 - [18] H.G. Bouanani, D.Eddike, B.Liautard, G.Brun, *Mater. Res. Bull.* 31, 2, 177-187, 1996.

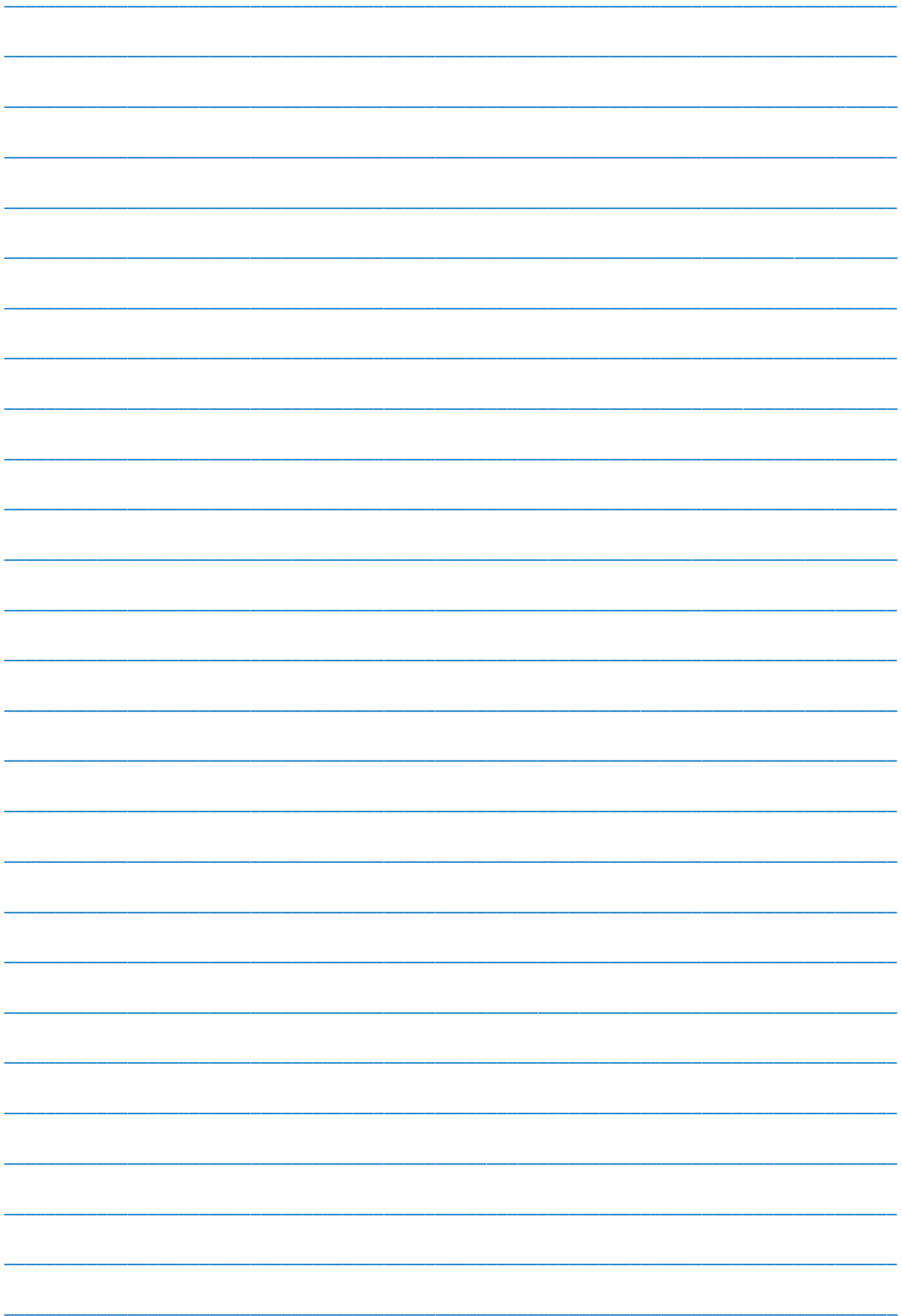
Received: 19.06.2019

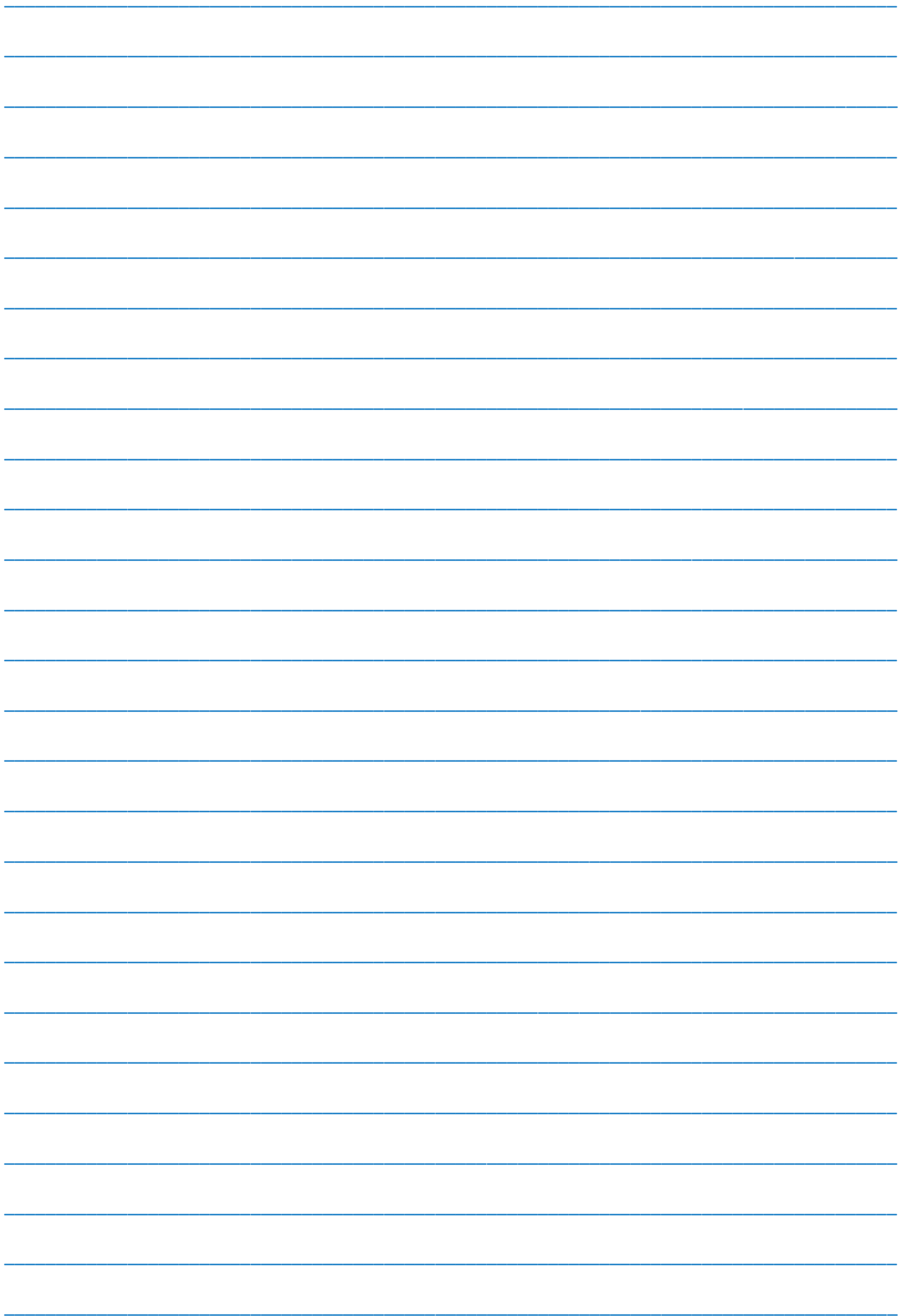












CONTENTS

1.	The low-frequency dielectric properties of benzene-bromobenzene system S.T. Azizov, O.A. Aliyev, R.G. Abaszade	3
2.	Electronic structure of the Ge vacancies in GeSe layered semiconductor Z.A. Jahangirli, B.H. Tagiyev, S.A. Nabiyeva	6
3.	The structural analysis and thermal power of $\text{Bi}_2\text{Sr}_2\text{CaCu}_2\text{O}_x$ and $\text{Bi}_2\text{Sr}_2\text{Ca}_{0.6}\text{Zn}_{0.4}\text{Cu}_2\text{O}_x$ S.S. Ragimov, G.I. Agayeva	10
4.	Semiconductors with deep traps in strong electric and magnetic fields E.R. Hasanov, Sh.G. Khalilova	13
5.	Transport properties of solid solution $(\text{AgSbTe}_2)_{0.8}(\text{PbTe})_{0.2}$ S.S. Ragimov, M.A. Musayev, N.N. Hashimova	18
6.	Photosensitivity features of electrophotographic layers of CdInGaS_4 V.G. Agayev	20
7.	Dependence of electron mobility on their surface density in a semiconductor quantum well with the modified Poschl -teller confining potential M.M. Babayev, X.B. Sultanova, M.Q. Abbasli	22
8.	Photoluminescence properties of $\text{Ni}_{1-x}\text{Zn}_x\text{Fe}_2\text{O}_4$ nanopowders Sh.A. Ahmadova, T.G. Naghiyev, Sh.N. Aliyeva, A.A. Sadigova, T.R. Mehdiyev	25
9.	Simulation spatial structure of amyloid beta-peptide (31-35) determined by molecular mechanic method G.A. Agaeva, G.Z. Najafova, N.M. Godjaev	31
10.	Synthesis and characterization of $\text{BiTe}_{1-x}\text{Se}_x\text{I}$ solid solutions series Ziya S. Aliev	37



www.physics.gov.az